Silicon radiation detectors. A study of processing parameters and radiation hardness

Andreas Werner

II

Preface

This is a thesis for the Cand.Scient degree at the Department of Physics, University of Oslo. The thesis is based on work done in the period from new year 1998 to the spring of 1999. The work was done at CERN and at SINTEF Electronics and Cybernetics, Department of Microsystems.

Prof. Steinar Stapnes at the Department of Physics was my main supervisor. During the one and a half year he has never stopped being an encouraging supervisor, and his comments and corrections in the process of writing my thesis have been a great help to me.

Research Scientist Berit Sunby Avset was my supervisor at SINTEF. She helped me start the diode experiments, and was always there to help and give inspiration.

Shaun Roe, Petra Riedler, and the others at the Solid State Detector Group at CERN took always good care of me, and was helpful when I had problems at their laboratory. A special thanks to Bob Boulter who had to live with my constant nagging during the detector annealing, and still quickly repaired whatever I broke.

Then a special thanks to the people at the Department of Microsystems for making my stay there both socially and professionally interesting.

Blindern, May 19, 1999

Andreas Werner

Contents

Chapter 1

Introduction

Silicon radiation detectors are used in most large particle physics experiments today. These detectors can be manufactured to give excellent resolution and fast readout, and are therefore well suited for an experiment like LHC, where a high interaction rate will give annual radiation doses equivalent to $\sim 10^{13}$ neutrons/cm^2/year.

These high radiation levels will lead to damages in the silicon, damages that degrades the performance of the detectors. A comprehensive R&D program inside the collaboration at CERN has explored the performance of irradiated detectors. First n-in-n detectors were the technology choice for all the ATLAS silicon detector systems, but later the p-in-detectors have been studied. An experiment[11] showed that p-in-n detectors could replace n-in-n detectors in the ATLAS silicon strip system. These detectors are easier to produce and cheaper than n-in-n detectors, and has become to technology choice for the ATLAS microstrip system.

A p-in-n detector produced at SINTEF had specially low depletion voltage compared to the rest of the detectors, and some hypotheses to explain this was put forward. In this thesis several studies have been performed on irradiated detectors with different processing parameters. These detectors leakage current and depletion voltage have been compared with each other and earlier experiments, to find out what might cause these effects.

The experiments and results are described later in this thesis, but I will first give an introduction to the purpose of these detectors and the experiments they will be put into at CERN.

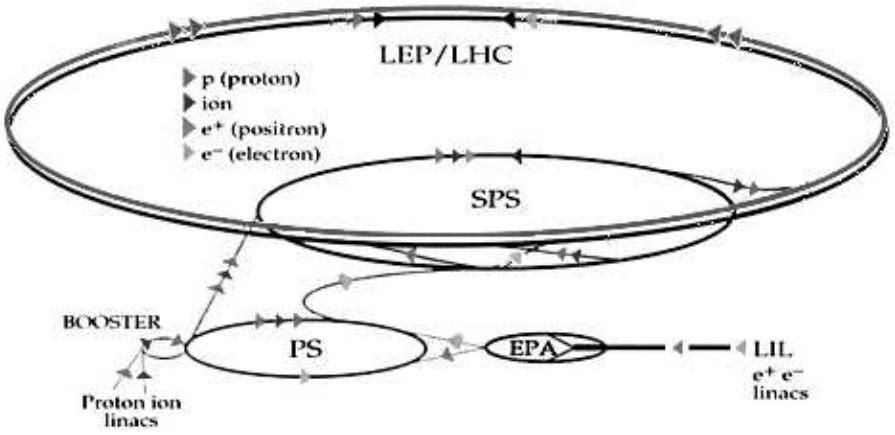

Figure 1.1: Accelerators at CERN

1.1 CERN

CERN is the European Laboratory for Particle Physics, the world largest particle research center. It was officially formed on the 29th September 1954 under the name "Conseil Europeen pour la Recherche Nucleaire". The creation of this laboratory was recommended at an UNESCO meeting in Florence in 1950 as the only way forward for front-line particle physics research in Europe. The convention was signed in 1954 by 12 countries, and membership have today grown to the present 19 member states. In addition 4 countries, the European Commission and UNESCO have observer status.

1.1.1 Accelerators

There are today three major accelerators at CERN.

- PS, the Proton Synchrotron
- SPS, the Super Proton Synchrotron
- LEP, the Large Electron Positron collider

Figure 1.1 gives an overview of these three accelerators and all other accelerators at CERN. The SC, the Synchro-Cylotron was the first accelerator at

CERN. The next accelerator was the Proton Synchrotron which was completed in 1959. This accelerator is still in much use today as an injector to the Super Proton Synchrotron, SPS. The SPS is in its turn the injector to the Large Electron Positron accelerator, LEP. In addition to being injectors to other accelerators both the PS and the SPS also work as important radiation sources for other types of experiments, such as solid state physics. LEP has a circumference of 27 km and is for the moment the largest accelerator at CERN, and it will remain so until it is taken apart for the construction of the LHC. The LEP accelerator accelerates two beams of positrons and electrons in opposite directions until proper energies is achieved. The beams are then allowed to collide in different experimental areas. LEP started at energies round 91 GeV to produce Z_0 particles, and since 1995 the energy has been doubled to allow:

- the study of W^+W^- pairs
- extended search of new particles, in particular the Higgs boson

In October/November 1996 LEP was working at 172GeV. LEP has four experimental areas around its circumference, and each area contains a particle detector. The detectors are named DELPHI, ALEPH, L3 and OPAL.

1.2 Physics

The Standard Model describes the interaction between matter with two types of fundamental particles, bosons and fermions. Bosons are force carriers that have integer spin, and fermions are matter particles that have half integer spin. Fermions are grouped into two families of particles, leptons and quarks, as shown in table 1.1. The leptons can exist by themselves, while the quarks always cluster together. Protons and neutrons are the most common of these clusters, called hadrons. As mentioned the bosons are force carriers, and each type of bosons is connected to one basic force:

- Photons (γ's) carry the electromagnetic force
- W^+, W^- and Z_0 are carriers of the weak force
- Gluons are carriers of the strong force.

Table 1.1: The Standard Model

FERMIONS			*BOSONS*
Leptons			*Gauge bosons*
Electron	Muon	Tau	W^+W^-
Electron neutrino	Muon neutrino	Tau neutrino	Z_0
Quarks			Photon
Up	Charm	Top	Gluon
Down	Strange	Bottom	

The different particles cover a wide range of masses, from massless(γ) to masses about the same as a gold-nucleus(top). Why there is such a range of masses and how particles get masses at all are not well understood. The Standard Model explains the masses trough the Higgs mechanism. In this theory all particles, both matter particles and force carriers, interact with the Higgs boson. The strength of the interaction gives rise to mass, the stronger interaction, the greater the mass. The Higgs boson(s) has not been found, and new experiments have to be done to show whether this model is correct.

The Universe seems to consist of purely matter while most fundamental reactions are matter/antimatter symmetric. The observed asymmetry is thought to come from a breakdown of symmetry between particles and antiparticles, known as CP-violation in electroweak reactions. This has been observed for neutral kaons, which contain the strange quark of the second-generation. If the theory is correct particles containing bottom quarks should also reveal this symmetry breaking.

Another goal for particle physics is to unify the electroweak theory with the strong force, and make a so called Grand Unified Theory (GUT). This unification of electromagnetic, weak and strong force is thought to take place at energies much higher than particle accelerators can reach. Even more important is to study models where gravity can be described as a quantum field theory. Typically the theories require that Nature has a deep symmetry known as supersymmetry (SUSY). Supersymmetry links the matter particles with the force-carrying particles and implies that there are additional superparticles necessary to complete the symmetry. These super particles must be much heavier than their ordinary partners, since they have not been observed.

1.3 LHC

The LHC, Large Hadron Collider, is the next research instrument in Europes armory. It is designed to to fit into the 27 km LEP tunnel, and be fed by existing particle sources. It will be filled with protons delivered from the SPS and are pre-accelerated to 0.45TeV. Two superconducting magnetic channels will accelerate the protons to 7-on-7 TeV, after which the beams will counter rotate for several hours, colliding at experiments, until they become so degraded that the machine will have to be emptied and refilled. The LHC will consist of 5 000 superconducting magnets that that are used to guide and collide the beams. The most extreme of these magnets are the bending magnets that will be able to produce fields of 8.36 Tesla, and makes it possible to bend the 7 TeV protons around the ring.

1.3.1 Experiments

Four large scale experiments will be situated round the LHC. These experiments, shown in figure 1.2, are named ALICE, ATLAS, CMS and LHCb. ATLAS and CMS are general-purpose machines that are designed to study the wide range of physics opportunities offered by LHC:

- Search for and study of new physics
  - Origin of EW symmetry breaking
    - Higgs boson
    - Alternatives
  - SUSY
  - Compositeness
  - Leptoquarks
- Measurements
  - top mass and decay properties
  - B-physics
  - Cross sections, etc.
    - W,Z,γ production
    - jets

    * hadronic production

LHCb is a dedicated B-physics experiment, and will together with the two general purpose experiments look at B-physics:

- CP violation
- B_s^0 oscillations
- Rare decays
- Doubly-heavy mesons, etc.

ALICE is a different kind of experiment, the colliding particles are lead atoms, not protons. This experiment study quark-gluon plasma, quarks and gluons that are to hot to stick together, as in the early universe.

Each experiment, or detector, is designed to detect particles that are created from collisions of particles with high energy. The newly created particles have properties that are typical for those types of particle, ie. mass, charge and momentum. The experiments consist of several sub detector systems that have different purposes. The inner part measures the trajectory of a particle in a magnetic field, and on the outside there are several calorimeters that measures the energy of different types of particles. Outside the calorimeters the muons are identified and measured in magnetic field. A schematic LHC detector is shown in figure 1.3. The detector measures momentum and charge of charged particles, energy and direction of photons and electrons, energy and direction of jets of hadrons, charge and momentum of muons and finally missing transverse energy.

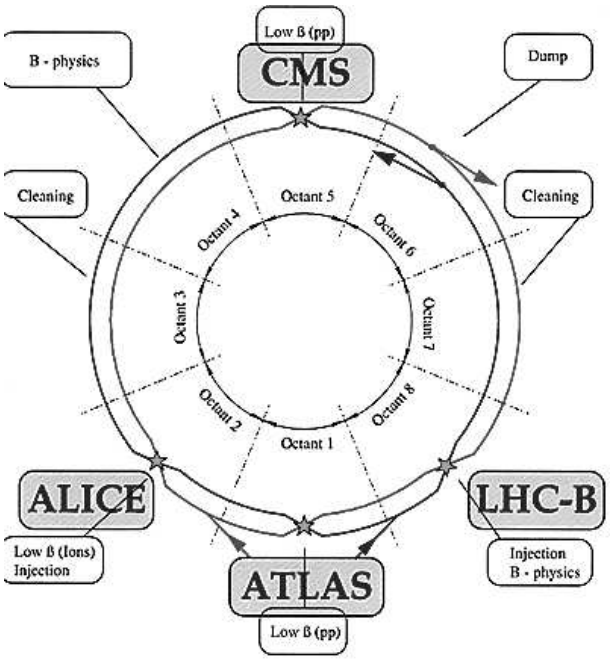

Figure 1.2: Experiments at LHC

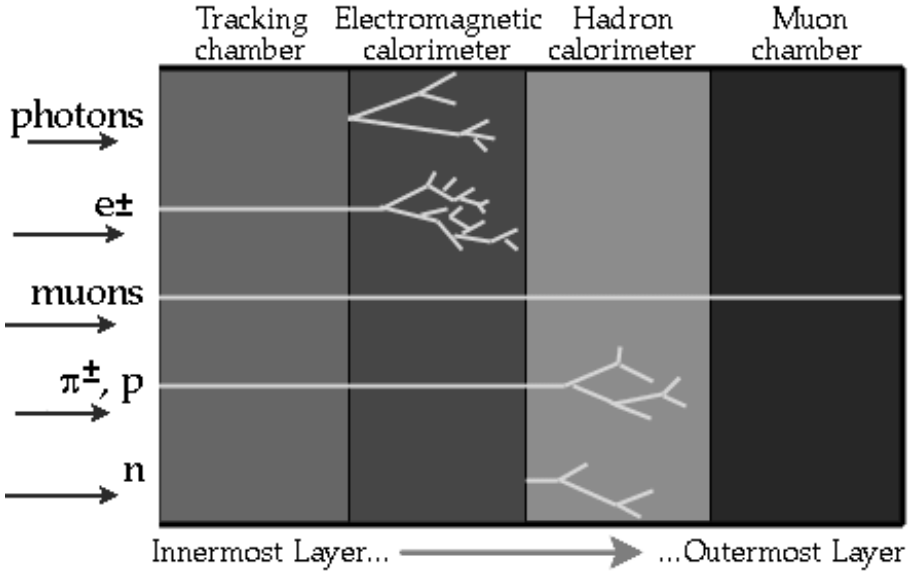

Figure 1.3: A simplified LHC detector

Chapter 2

Atlas

2.1 Overview

The ATLAS detector consists of four major components that all can be seen in figure 2.1. In the center of the detector the inner tracker tracks the particles in a magnetic field. The reconstruction of these tracks gives the possibility of vertex detection, and of measuring the momentum of each charged particle. The inner tracker will be described in more detail in section 2.2.

Outside the inner tracker the calorimeter measures the energies carried by the particles. The calorimeter consists of alternating metal plates (absorbers) and sensing elements. Interaction in the absorbers transform the incident energy to particle showers that are detected by the sensing elements. The ATLAS calorimeter has two parts, the EM calorimeter and the hadronic calorimeter. The EM calorimeter uses lead absorber plates, and the sensing elements are filled with liquid argon. The showers in argon liberate electrons that are collected and recorded. The hadronic calorimeter is based on plastic scintillator tiles embedded in an iron absorber. The scintillating tiles emit light when the showers pass them, and the light is detected with photomultipliers which then give an electronic signal that is recorded.

The mouns have a small cross section, and are therefore not stopped in the calorimeter. So outermost there is a muon spectrometer that identifies and measures muons. The muon spectrometers precision measurements are provided with two system, Monitored Drift Tubes and Cathode Strip Chambers. The muon spectrometer is also an important part of the ATLAS trigger

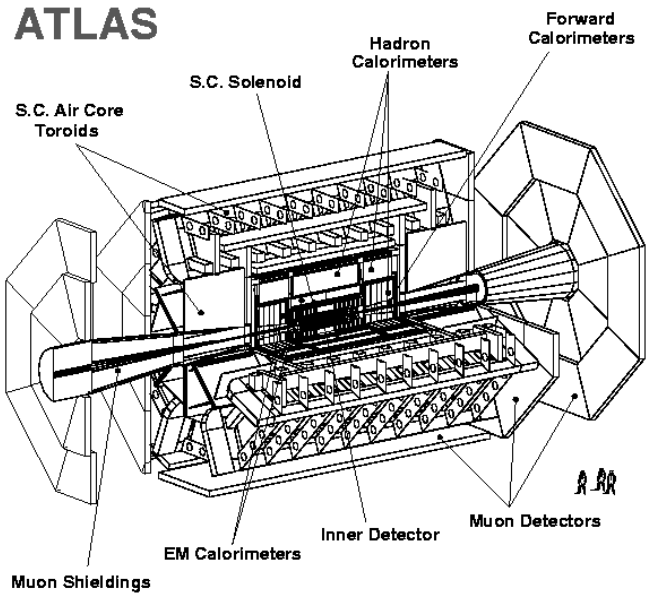

Figure 2.1: The ATLAS detector

system, and a dedicated trigger system has been built in the spectrometer. This system uses Resistive Plate Chambers in the barrel region, and Thin Gap Chambers in the end-cap region.

The fourth component is not a detector, it is the magnets that are used to find the momentum and charge of the particles. The detector has three magnet systems. All magnets are superconductive and therefore need cooling to liquid helium temperature. The central solenoid provides $2T$ in the central tracking volume. The other two systems are part of the muon spectrometer. The magnetic field of the barrel toroid and the two end-cap toroids provides bending powers of $3Tm$ and $6Tm$, respectively.

The LHC will give a $40Mhz$ interaction rate in the detector. At this rate it is impossible to read out and store all information obtained in the detector, and since only a small fraction of the detector hits are interesting, some selection of interesting events has to be done. A three level trigger and data acquisition system has been developed to meet this task. The first level trigger is hardware based and works on a a subset of information from the calorimeter and muon detectors. It requires about $2\mu s$ to reach a decision, and reduces the rate to $100kHz$. The second level trigger has $10ms$ to reach a decision, reduces the rate to $1kHz$. The level two trigger uses

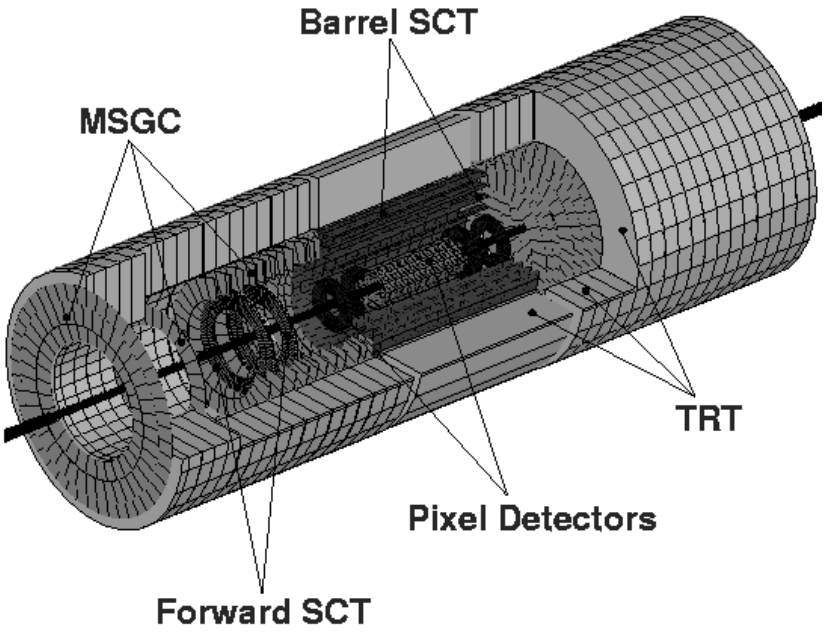

Figure 2.2: The ATLAS inner detector

the information from the first level trigger, but refines that levels selection of candidate objects using full granularity information from all detectors. The level three trigger is a complete event reconstruction using processor farms, and the data are sent to mass storage at a rate of $10Hz$.

2.2 Inner Detector

The purpose of the inner detector is to track charged particles from the collision point to the electromagnetic calorimeter system. Since a very large track density is expected at the LHC fine granularity detectors are needed. Three different detector systems are put together to reach the specified momentum and vertex resolution. These systems consist of pixel detectors, microstrip detectors and straw detectors. The Inner Detector has an outer radius of $115cm$ and a total length of $7m$, and consist of three units, a barrel region and two identical end caps. All these parts can be seen in figure 2.2.

The pixel detectors are designed to give high precision measurements as close to the interaction point as possible, the closest barrel detector layer situated at radii $4cm$. In addition there are two more barrel layers and four disks on each side. The resolution of the barrel layers is $12\mu m$ in $R\phi$ and $66\mu m$ in z. With end cap disk, with resolution $12\mu m$ in $R\phi$ and $77\mu m$ in R, this systems precision measurements gives a resolution good enough to find short lived particles such as b-quarks and τ-leptons.

The microstrip detector system that is positioned between the pixel system and the TRT is described in more detail in section 2.3.

The Transition Radiation Tracker is referred to as a continuous tracking system. It is based on the use of straw detectors with xenon gas between the straws. This system allows a large number of measurements , typically $\sim$ 36, to be made on each track. Each channel provides two independent thresholds and allows the the detector to discriminate between tracking hits and transition radiation hits. The TRT then aids the pattern recognition by adding around 36 hits per track, and allows a simple and fast level-2 trigger to be implemented.

2.3 SemiConductor Tracker

The SemiConductor Tracker(SCT) is designed to provide four precision measurements per track in the intermediate radial range, contribution to the measurement of momentum, impact parameter and vertex position. The barrel SCT has four layers of silicon microstrip detectors to provide precision points in the $R\phi$ and z coordinates, and nine disks in each of the forward and backward directions to the provide $R\phi$ and R coordinates. The resolution is $16\mu m$ in $R\phi$ and $580\mu m$ in z, and $16\mu m$ in $R\phi$ and $580\mu m$ in R for the respective two systems.

In the barrel region the detectors are rectangular with the overall size $64 \times 63.6mm^2$. The active area of the detector is $62 \times 61.6mm^2$ with 768 strips of $80\mu m$ pitch. Each strip is AC-coupled, and the detector will be negative-biased from the backside to maintain only a small voltage across the capacitor oxide. A simplified layout of this detector is shown in figure 2.3.

A barrel layer consists of modules that are made out of four detectors. Two detectors are daisy-chained for each side of a module, and the result is

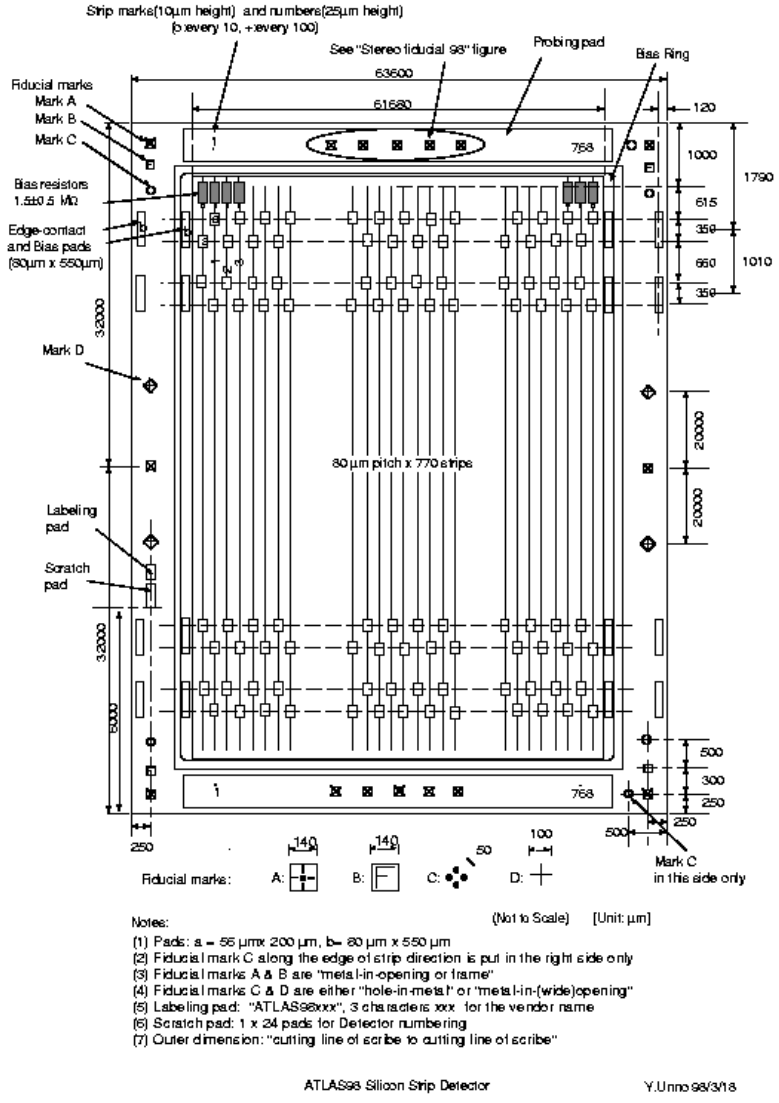

Figure 2.3: Layout of the SCT Barrel Detector

a detector with 768 strips of $80\mu m$ pitch and $112.3mm$ active length. These detectors are then glued back to back with a identical pair rotated by $40mrad$, to provide z-measurement capability. In the barrel region the front end ICs are bonded at the middle of the module to minimize the effect of fan-out capacitance on the S/N, and the strip resistance. In the forward regions the mechanical assembly is more complex, and the ICs are bonded in one end of the module.

The front-end electronics is based on a binary readout architecture. A strip that collects charge above a certain threshold fires a per strip discriminator and the output is stored in a pipeline until a trigger initiates readout for that beam-crossing.

Chapter 3

Silicon detectors

When charged particles pass trough a semiconductor many electron-hole pairs get produced along the path of the particle. The average energy that the incoming particle lose to produce one electron-hole pair is called the ionization energy, ϵ. The ionization energy is not completely independent of the energy and type of the incoming particle, but in most cases it can be approximated to be constant. For silicon ϵ is about 3.6eV. In a gas filled detector the ionization energy is about 30eV, and the silicon detector therefore gets ten times more charge carriers for a given energy deposited in the detector. The high number of charge carriers increases the S/N-ratio. A high S/N-ratio increases the energy- or position resolution depending on the purpose of the detector. Other desirable features of semiconductor detectors are compact size, fast timing characteristics, and an effective thickness that can be varied to match the requirements of the application.

Some knowledge of semiconductor physics is helpful to understand the details of a silicon radiation detector. This chapter therefore starts with an introduction to this physics, followed by a more detailed description of silicon radiation detectors later in the chapter.

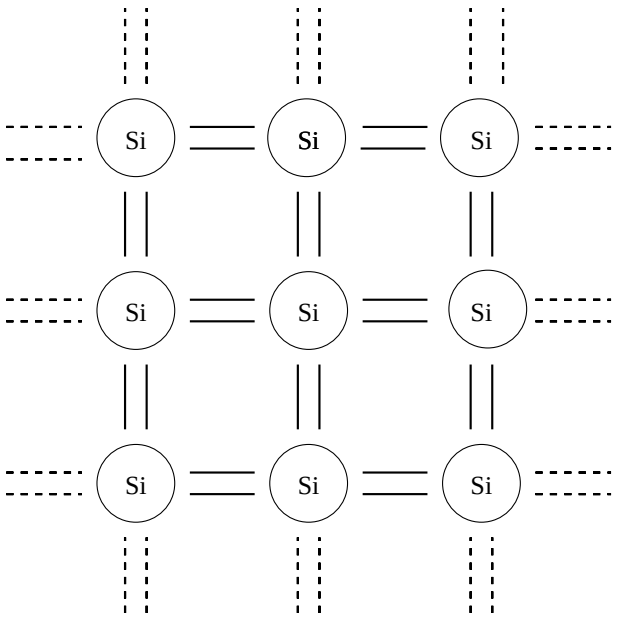

Figure 3.1: Two-dimensional representation of the intrinsic silicon lattice

3.1 Semiconductor physics

3.1.1 Silicon properties

Silicon is a group IV element in the periodic table and has a diamond crystal structure. The diamond lattice of silicon has the important characteristic that any atom within the structure have four nearest neighboring atoms. In a pure silicon crystal the atoms are bonded together with covalent bondings. The intrinsic silicon lattice can be represented in two dimensions like in figure 3.1. The periodic lattice of silicon establishes allowed energy bands for electrons that exist within the crystal. The energy of an electron has to be within the limits of a band. Between these bands there are gaps or ranges of forbidden energy. A simplified representation of the interesting bands is shown in figure 3.2. The lower band, the valence band, corresponds to the electrons that are bound to specific lattice sites within the crystal. The other band, the conduction band, represents electrons that are free to move trough the crystal.

At any nonzero temperature, some thermal energy is shared by the electrons in the crystal. It is then possible for a valence electron to gain enough

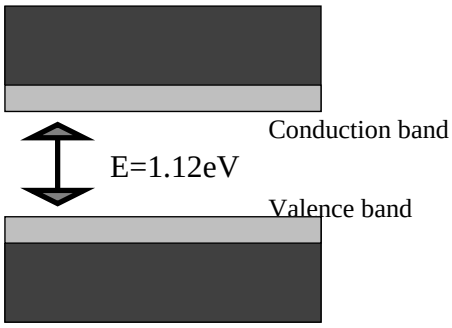

Figure 3.2: Band structure for electron energies in silicon

energy to be elevated across the band gap into the conduction band. Physically this represents the excitation of an electron from its covalent bond in the lattice. This electron can then drift trough the crystal. When an electron is created in the conduction band a vacancy, hole, is left in the valence band. The combination of these two is called an electron-hole pair. The probability per unit time that an electron-hole pair is thermally generated is given by:

$$p(T) = CT^{3/2} exp - \frac{E_g}{2kT} \tag{3.1}$$

where T is the absolute temperature, E_g is the band gap energy, k is the Boltzmann constant and C is a proportionality constant characteristic of the material.

Both the electron and the hole will move if an electric field is applied to the semiconductor material. This motion will be a combination of a random thermal velocity and a net drift parallel to the direction of the applied field. The electrons move in the opposite direction of the field vector, holes move in the same direction as the electric field. This means that the hole is a positive charge and is what was expected since a hole actually represents the absence of a negatively charged electron. The drift velocity, v, of electrons and holes can be described by equation 3.2 and equation 3.3, respectively

$$v_e = \mu_e \varepsilon \tag{3.2}$$

$$v_h = \mu_h \varepsilon \tag{3.3}$$

where μ_e is the mobility of electrons and μ_h is the mobility og holes. These two equations are only valid for low to moderate values of the electric field intensity. For sufficiently large electric fields will a saturated drift velocity be reached. For both charge carriers this velocity is about $10^7 cm/s$.

In a completely pure semiconductor the electron-hole pairs would be the only electrons and holes in the conduction band and the valence band, respectively. This is called an intrinsic semiconductor. This is not the case for real semiconductors were small levels of impurities dominate the electrical properties. For an intrinsic semiconductor the number of electrons and holes are equal, and from equation 3.1 we can see that we get the lowest concentrations at a low temperature and a large band gap. For silicon at room temperature the intrinsic electron and hole density is $1.5 \times 10^{10} cm^{-3}$.

If one of the silicon atoms is replaced with a atom of another material the electrical properties of the silicon crystal can change. Normally small concentrations of impurity of group V or group III of the periodic table are added to the material. The group V atoms have five valence electrons and when taking the site of a silicon atom in the lattice one electron will be left over after the covalent bonds have been formed. This is illustrated in figure 3.3. The extra electron is only lightly bounded to the impurity site, and it therefore takes very little energy to elevate the electron into the conduction band and leave behind a positively charged phosphorus ion. The impurity atom donates an electron to the conduction band, and is therefore called a donor impurity atom. These atoms are not part of the regular lattice and can therefore occupy a position in the forbidden band gap. The electrons will have energies near the top of the gap as shown in figure 3.4.

The group III atoms, such as boron, have only three valence electrons which are all taken up in the covalent bonding. As shown in figure 3.5 this gives an empty covalent bonding position. The electron occupying this position would have an energy greater than that of the valence electrons. That is because the net charge state of the boron now would be negative. This electron has not enough energy to be in the conduction band, so its energy is far smaller than the conduction band energy. A valence electron may gain a small amount of thermal energy an move in the crystal, this electron occupies the empty site, and another valence electron get vacated. These other electrons may be thought of as holes in the silicon. These impurities are called acceptor impurities since the impurity accepts a electron from the valence band. The holes will have energies near the bottom of the gap as shown in figure 3.6.

The acceptor atom generates holes in the valence band without generating electrons in the conduction band. The hole is positively charged and is therefore referred to as p-type material. The donator adds electrons to the conduction band without creating holes in the valence band. The electrons

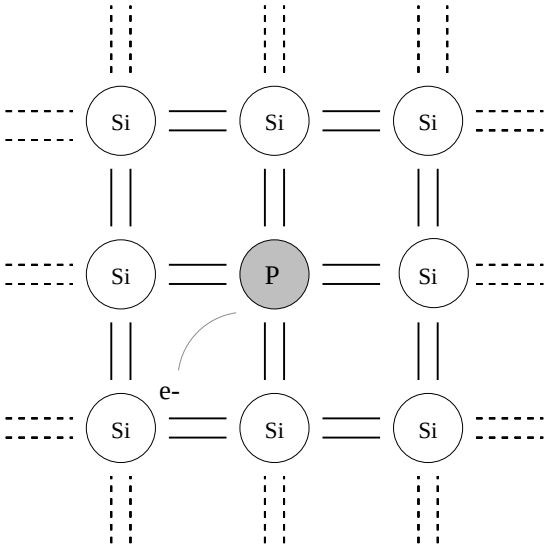

Figure 3.3: Two-dimensional representation of the silicon lattice doped with a phosphorus atom

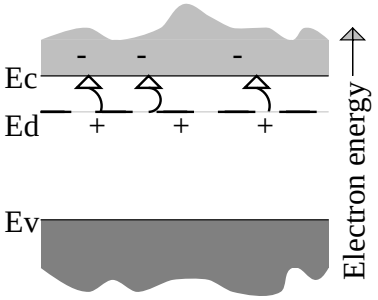

Figure 3.4: Energy band diagram of phosphorous doped silicon

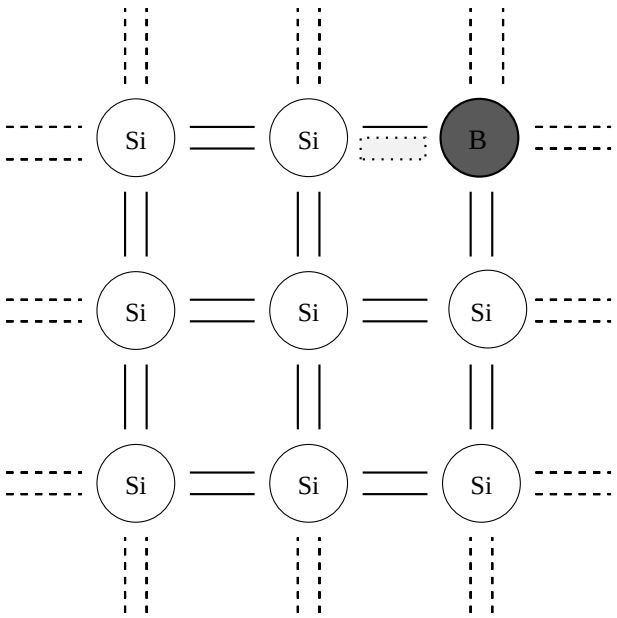

Figure 3.5: Two-dimensional representation of the silicon lattice doped with a boron atom

are negatively charged and the material is referred to as n-type material.

Both n-type and p-type materials have the property that the energy between the impurity energy levels and the bottom or top of the energy gap is small. The probability of thermal excitation given by equation 3.1 is then large. In most cases the concentration of the impurity is much larger than the intrinsic concentration. The number of conductors, holes or electrons, then become completely dominated by the contribution from the impurities. The added concentration of impurities increases the rate of recombination, shifting the equilibrium between electrons and holes. As a result the equilibrium concentration of the minority carrier decreases by an amount such that the equilibrium constant given by the product of n and p is the same as for the intrinsic material, equation 3.4.

$$np = n_i p_i \tag{3.4}$$

Electronic carriers that are formed in the semiconductor will migrate either spontaneously or under the influence of an electric field. The lifetime of the carrier is the time from its formation until it recombines. In a perfectly pure semiconductor the average lifetime of charged carries could be as large

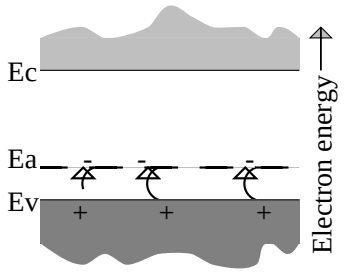

Figure 3.6: Energy band diagram of boron doped silicon

as a second, but in practice much smaller values are observed. This is caused by low level impurities, such as gold, zinc, cadmium or other metallic atoms, remaining in the material. These impurities introduce energy levels near the middle of the band gap, and are therefore classified as deep impurities. Acceptor and donor impurities are classified as shallow impurities because the energy levels of these impurities lie near the edges of the band. The deep impurities can capture charge carriers for a relatively long period of time. This immobilizes the carrier and these impurities is therefore referred to as traps. Another type of deep impurities is a recombination center. These impurities are able to capture both an electron and and a hole and thus causing them to annihilate. Instead of the theoretical value of about one second real lifetimes are at least three or four orders of magnitude smaller than that.

3.1.2 The pn junction

To illustrate a pn-junction two semiconductor crystals of p and n types are brought together. The crystals have impurity concentrations N_a and N_d, respectively. The difference in the concentration of electrons and holes between the two materials will start a diffusion of holes towards the n-region, and a diffusion of electrons in the other direction. The diffusing electrons will fill up holes in the p-region while diffusing holes capture electrons on the n-side. Since the regions initially are neutral this recombination causes a charge to build up on both sides of the junction. This creates an electric field gradient across the junction, witch after some time stops the diffusion. This is illustrated in figure 3.7. The electric field rises a potential difference across the junction known as the contact potential. The region of changing potential is known as the depletion zone or space charge region. This field leaves the

space charge region completely empty of mobile charge carriers. The width of the depletion zone depends on the concentration of n- and p-impurities and can be found from Poissons equation:

$$\frac{d^2V}{dx^2} = -\frac{\rho(x)}{\varepsilon} \tag{3.5}$$

A uniform charge distribution is a simplification of a real distribution, but works well as an illustration. We then have

$$\rho(x) = \begin{cases} eN_d & 0 < x < x_n \\ -eN_a & -x_p < x < 0 \end{cases} \tag{3.6}$$

where N_d, N_a, x_p and x_n is the donor concentration, acceptor concentration, extent of depletion zone on p-side and extent of the n-side, respectively. Since the total charge is conserved the relation $N_a x_p = N_d x_n$ can be used. With this uniform charge distribution $dV/dx = 0$ at $x = x_n$ and $x = x_p$. From these equations and integrating equation 3.5 twice yields,

$$V(x) = \begin{cases} -\frac{eN_d}{\varepsilon}\left(\frac{x^2}{2} - x_n x\right) + C & 0 < x < x_n \\ \frac{eN_a}{\varepsilon}\left(\frac{x^2}{2} + x_p x\right) + C' & -x_p < x < 0. \end{cases} \tag{3.7}$$

The two solution must join at $x = 0$, so $C' = C$. At $x = -x_p$ is $V = 0$ and at $x = x_n$ is $V = V_0$, which defines the contact potential. The solution to equation 3.7 is then:

$$V_0 = \frac{e}{2\varepsilon}(N_d x_n^2 + N_a x_p^2) \tag{3.8}$$

From this it is possible to obtain,

$$d = x_n + x_p = \left(\frac{2\varepsilon V_0}{e}\frac{(N_a + N_d)}{N_a N_d}\right)^{1/2} \tag{3.9}$$

where d is the width of the depletion zone. If one side of the junction is more heavily doped than the other, then from equation 3.9 the depletion zone extend farther into the lighter-doped side. If $N_a \gg N_d$, then the width of the depletion zone is approximately:

$$d \approx \left(\frac{2\varepsilon V_0}{eN_d}\right)^{1/2} \tag{3.10}$$

If the pn junction is reverse biased, ie. a negative voltage to the p-side, the holes are attracted to the p-contact in the p-region and similarly for electrons in the n-region. In effect the depletion region is thus enlarged. Under reverse

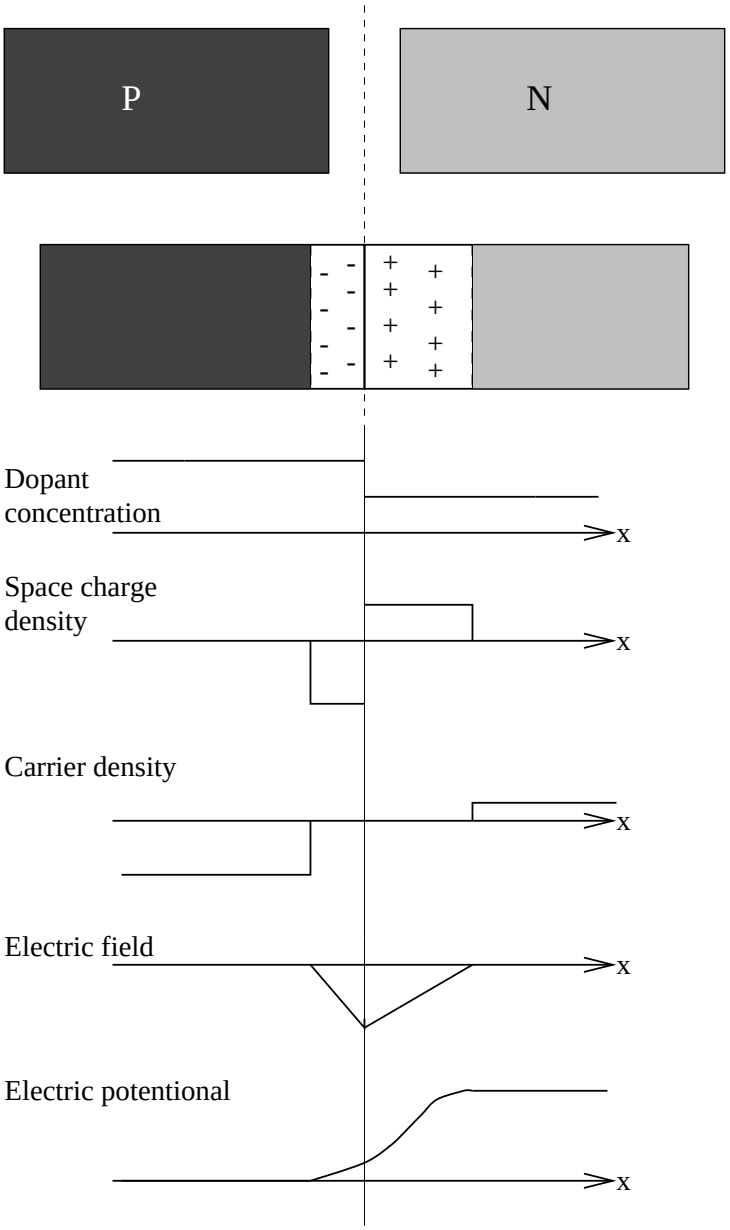

Figure 3.7: pn-junction

bias the width of the depletion layer can be calculated from equation 3.10 by replacing V_0 with $V_0 + V_B$, where V_B is the bias voltage. In most cases $V_0 \ll V_B$, so in the rest of this thesis V_B is neglected.

Another important property of the depletion region is the capacitance, which for a planar geometry is

$$C = \frac{\varepsilon}{d} \approx \left(\frac{e\varepsilon N}{2V_B}\right)^{1/2} \tag{3.11}$$

where C is the capacitance per unit area.

3.2 Semiconductors as radiation detectors

One possible approach to make a silicon radiation detector would be to take a piece of high restivity silicon, make contacts on two sides, and put an electric field over it. Equation 3.2 and equation 3.3 show that a high electric field is needed to get efficient collection of induced charge carriers, but a high voltage also introduces noise. Take as an example a piece of 1 mm thick silicon that is cut with a $1cm^2$ surface area. This piece is made of high purity silicon, which is the most common used for silicon detectors, with a restivity of about 5000Ω. The electric field is f.ex. $500V$, and since the silicon is connected with ohmic contacts the current, from Ohms law, through the detector is $0.1A$. This current corresponds to an equivalent charge of 6×10^{11} e/h pairs in a typical signal shaping time of $1\mu s$. A MIP induces 2.3×10^4 charge carriers in a $300\mu m$ thick silicon detector compared to the statistical fluctuations of around 10^6, and it would be practically impossible to detect that pulse.

The solution to this problem is the pn-junction. The pn-junction is an blocking electrode, that is, charge carriers removed by the electric field is not replaced at the opposite electrode. Ideally this would make a perfect detector with no other current than the one introduced by radiation induced charge carriers. Real silicon detectors, though, have two types of leakage current that introduce noise in the system, namely the reverse saturation current and the reverse-bias generation current. The reverse-bias generation current consist of thermally generated electron-hole pairs origination from trapping and recombination centers in the depletion region. This current is proportional to the width of the depletion region, and have a temperature dependence from equation 3.1. The reverse-bias generation current density is on the order of a few $\mu A/cm^2$, while the reverse saturation current is in the

range of nA/cm^2. The reverse saturation current comes from electron-hole pairs generated outside the depletion region. The electron and hole usually recombine, but when generated in the proximity of the depletion region the electron or hole has a chance of diffusing into it before recombination. The electron or hole are then swept away with the electric field and generates a current. The reverse saturation current is proportional to the area of the junction, but is usually neglected because of the much higher generation current.

A pn-junction, or pn diode, without reverse biasing will work as a detector, but not a very good one. The intrinsic electric field will not be intense enough to provide efficient charge collection and the small depletion thickness will also increase the noise in the signal output. Most detectors are therefore operated fully depleted, that is, the depletion region extends over the entire thickness of the detector. The full depletion voltage is from equation 3.10 then

$$V_{fd} = \frac{eND^2}{2\varepsilon} \tag{3.12}$$

where D is the thickness or the maximum depletion depth of the detector.

In the region that is not depleted no electric field exist, neither is any charge carriers collected in this area. This undepleted region also slows down the charge collection from the depleted region because it works as a serial resistance with high restivity. Fast charge collection is possible when there exist a electric field trough the entire volume of the detector, that is at full depletion voltage. With reverse biasing higher than the depletion voltage the detector is said to be over-depleted, and as shown in the figure 3.8 this gives a high electric field everywhere within the detector. These advantages of a high field trough the entire detector is the reason for why almost all detectors are operated over-depleted.

Semiconductor detectors have a small signal output and low noise electronics is important, particularly is preamplification needed before any further signal treatment can be done. These preamplifiers are charge sensitive, and the electronic noise from the detector is given as

$$ENC = e\frac{V_{rms}}{w}C \tag{3.13}$$

where C is the total input capacitance of the detector, w the average energy required to create an electron-hole pair, V_{rms} the average voltage noise level on the output, and ENC is the equivalent noise charge. From equation 3.13 it is clear that minimizing the input capacitance is very important

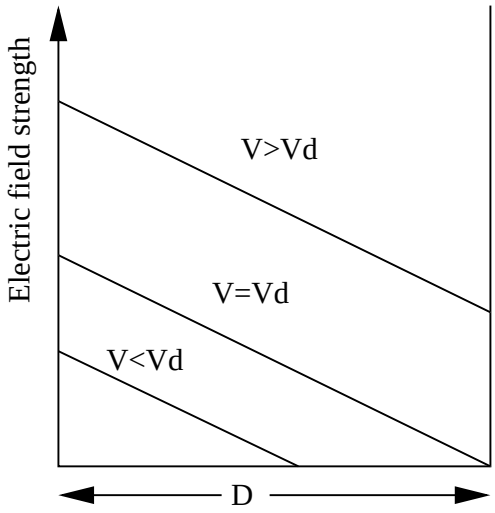

Figure 3.8: Electric field in a reverse biased silicon detector.

for the systems performance. The input capacitance, given in equation 3.11, is inverse proportional to the bias voltage and the minimum capacitance is obtained at full depletion voltage. This results in that the ENC has it lowest value when the detector is fully depleted, and is another reason to use fully depleted detectors.

3.3 Microstrip detectors

A simple diode as described in the previous section can detect a passing particle, but is not sensitive to where in the diode the particle passed. One can imagine to put a large number of diodes side by side to create a detector. If each of this diodes were read out individually, this would be a position sensitive particle detector, and the resolution of this detector would be equal to the size of each small diode. This is the basic idea of a pixel detector, but in practice it is easier to put all the diodes on one substrate. The pixel detector is produced on a silicon substrate with planar technology, which makes it possible to produce a large number of small diodes on one wafer. In ATLAS each pixel, or diode, have an area of $50\mu m \times 300\mu m$.

The planar technology also makes another, much simpler, approach possible. The pixels are replaced with long parallel strips and the result is a

microstrip detector. A corner section of such a silicon microstrip detector is shown in figure 3.9, and it is possible to see the strips, the bonding pads, the bias resistors and the guard structure. All these different parts of the detector have special purposes. The microstrips are the position sensitive detector elements, while the bonding pad on each end of the strip is the connection point for read out electronics. Each strip is biased trough a bias resistor that are connected to the bias line. The guard structure has several purposes, of which one is to conduct unwanted current, ie. due to surface states, outside the active area of the detector. Another is to prevent the depletion region of the outer strips to reach the edges of the detector. This prevents breakdown of the detector, and makes it possible for the outer strips to have the same uniform electric field as the strips in the middle of the detector. The processing of such a detector will be explained in more detail in section 3.3.1.

3.3.1 Processing of an ATLAS microstrip detector

The microstrip detectors that will be used in the ATLAS experiment are p-in-n detectors, p^+ strips on n type high restivity float zone silicon. The main steps of the planar process are shown in figure 3.10. The silicon wafer is first oxidized at approximately $1000°C$ to passivate the surface. Openings in the oxide are then made, using photolithographic and etching techniques, to enable implantation or diffusion in the desired areas. The figure show schematically the ion implantation that is followed by a new oxidation. The next step is a heat treatment that have two purposes, annealing of damages caused by the heavy ions and secondly gettering, the removal of impurities from the active detector area. Then the oxide on the backside of the detector is removed and both sides are metalized with aluminium. Photoprocessing is then used again to produce the strips on the frontside, and in the end the metal is sintered at about $500°C$. The processing of an ATLAS detector includes two additional processing steps. One of these steps is added between the ion implantation and the following oxidation, and is the processing of polysilicon bias resistors for the p^+ strips. Figure 3.11 show a cross section along the strip of such a structure. After all the processing steps shown in figure 3.10 is the the detectors frontside covered with some kind of passivation, typically polyimide. This is done to protect the aluminium strips, and is done with photoprocessing leaving only bonding pads and contact holes unprotected.

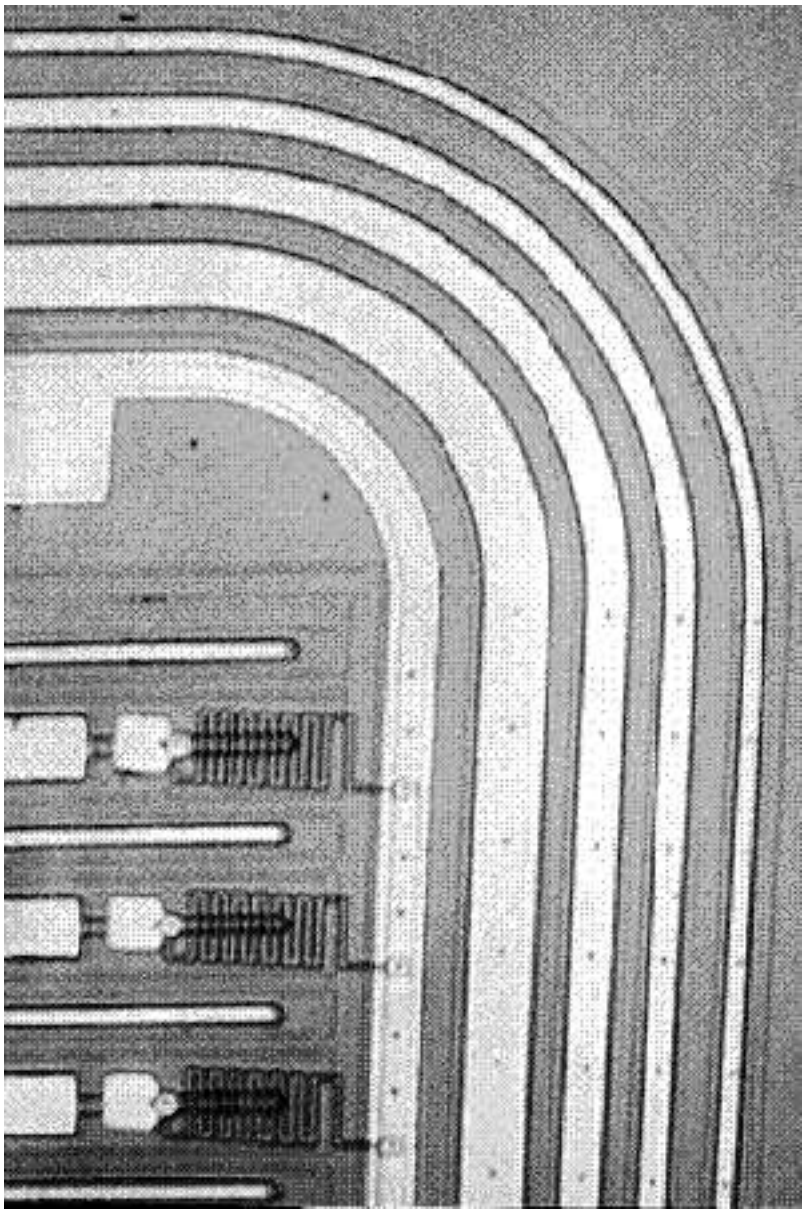

Figure 3.9: A corner section of an ATLAS silicon microstrip detector

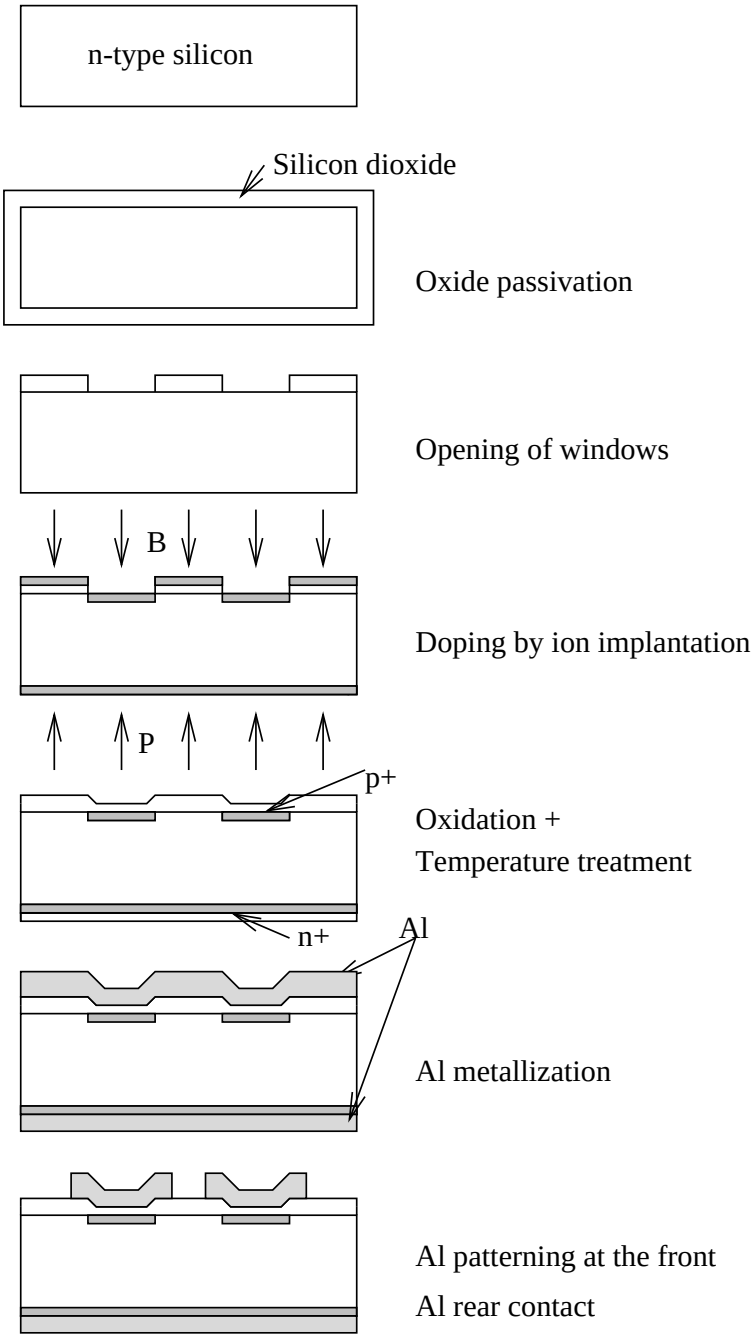

Figure 3.10: Planar processing of a silicon microstrip detector

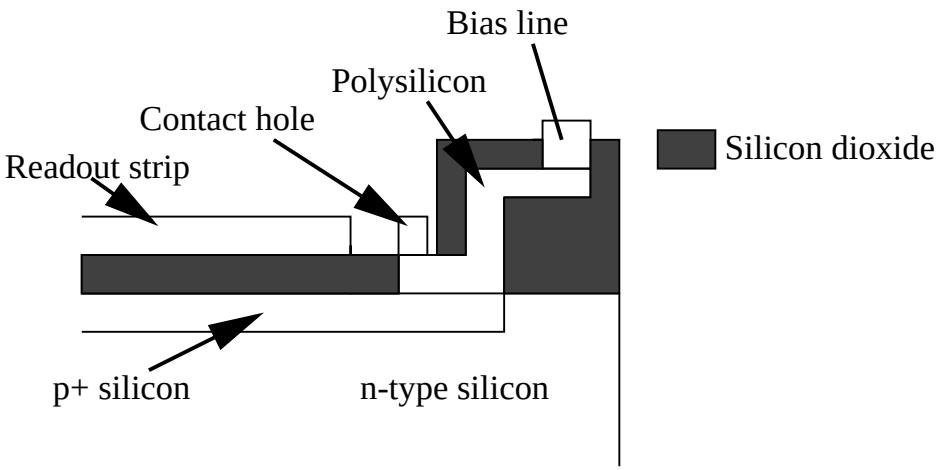

Figure 3.11: Cross section of a silicon detector with integrated coupling capacitors and polysilicon biasing resistors

3.4 Radiation effects

The continuous interaction with highly energetic particles will of course affect the properties of the silicon. Macroscopically an increase in the full depletion voltage and the leakage current are observed. After the irradiation both the full depletion voltage and the leakage current show a temperature dependent annealing behaviour. It is not well understood how the defects described in section 3.4.4 are linked to the macroscopical changes, so the only models that describes this are empirical models. In this section one of these models will be presented .

3.4.1 Type inversion

A effect not mentioned in the introduction of this section is the type inversion of the silicon. As described in section 3.1.1 and section 3.1.2 the space charge in an unirradiated device does result from shallow dopants in the silicon. The bulk damage caused by interacting particles introduces deep levels in the silicon, and results in an accumulation of negative space charge in the depletion region. The effective doping concentration, N_{eff}, can be expressed as [16]

$$N_{eff} = N_0 exp(-c\phi) + \beta\phi \tag{3.14}$$

where N_0 represents the initial dopant concentration, for an n-type device a negative number. ϕ is the fluence, c and β are temperature dependent constants. It has been shown that both constants have relatively large values, and thus indicates that the initial doping concentration only has minor effect on the full depletion voltage for fluences of more than a few times 10^{13}neutrons/cm^2. An n-type detector invert to effectively p-type at about 2×10^{13}neutrons/cm^2 and continues to become more p-type beyond this point. In a p^+n detector the electric field is extending from the p^+ into the bulk, so even when only partially depleted it is possible to obtain position information from the detector. When the detector is inverted the electric field extends from the n^+-side of the detector. This side have no strips, and if the detector is not fully depleted the position information is not good. The temperature dependence of c and β indicates that keeping the detectors at low temperature during irradiation will lower the effect of the radiation.

3.4.2 Depletion voltage

With a little change in equation 3.12 can the full depletion voltage be written as

$$V_{Dep} \approx \frac{qD^2 \mid N_{eff} \mid}{2\epsilon_S} \tag{3.15}$$

where ϵ_S is the permittivity of silicon and D is the detectors full depletion depth. The value obtained from this equation gives the initial depletion voltage after irradiation, which can be rather high. After irradiation, though, the depletion voltage starts to anneal. The annealing can be separated into short term and long term effects described with time constants τ_S and τ_L, respectively. Both time constants are strongly temperature dependent and increase with decreasing temperature. The time constant τ_S is assumed to describe an exponential decay of active acceptor sites created during the irradiation back to neutral inactive sites. The change in full depletion voltage caused by this effect at a time t after irradiation can be described with equation 3.16, where V_Z is related to a stable acceptor concentration produced during the irradiation process. V_Z is therefore the minimum value of the full depletion voltage.

The short time, or beneficial, annealing period can then be described by the term:

$$V_{Dep}(t) = V_Z + V_S exp(-t/\tau_S) \tag{3.16}$$

The long term contribution to the depletion voltage in equation 3.18 is described by equation 3.17, where V_A is related to a concentration of damage sites that can become activated acceptor sites,

$$V_A(1 - exp(-t/\tau_L)). \tag{3.17}$$

Since the short term annealing reduces the depletion voltage this annealing is often referred to as beneficial anneal. The long term contribution increases the depletion voltage and is referred to as anti-annealing. The time dependence of the depletion voltage is the superposition of equation 3.16 and equation 3.17 and is given as[16]

$$V_{Dep}(t) = V_Z + V_S exp(-t/\tau_S) + V_A(1 - exp(-t/\tau_L)) \tag{3.18}$$

As earlier stated the time constants are temperature dependent and are expressed as [16]

$$\tau_S(T) = 70exp(-0.175T) \tag{3.19}$$

$$\tau_L(T) = 9140exp(-0.152T) \tag{3.20}$$

where T is the temperature in $°C$.

V_Z, V_S and V_A are linear functions of the fluence ϕ, and can be written as:

$$V_S = \phi v_S \tag{3.21}$$

$$V_A = \phi v_A \tag{3.22}$$

$$V_Z = \phi v_Z \tag{3.23}$$

v_Z, v_A and v_S have been measured on silicon PIN diodes irradiated with protons. For 300μm thick detectors they have the following values[16]:

$$v_Z = 1.06 \times 10^{-12} Vcm^2$$

$$v_A = 3.8 \times 10^{-12} Vcm^2$$

$$v_S = 1.34 \times 10^{-12} Vcm^2.$$

3.4.3 Leakage current

The detectors leakage current increases significantly during irradiation. Current is described by leakage current per unit volume, J_V. The increase in J_V has been found to be directly proportional to the particle fluence [15]:

$$\Delta J_V = \alpha\phi \tag{3.24}$$

Table 3.1: Main reactions in defect kinetics modelling

I **reactions**	V **reactions**	C_i **reactions**
A)Diffusion reactions		
$I + C_S -> C_i$	$V + O -> VO$	$C_i + C_S -> CC$
$I + V_2 -> V$	$V + P -> VP$	$C_i + O -> CO$
$I + VP -> P$	$V + VO -> V_2O$	$CO + I -> COI*$
$I + V_3O -> V_2O$	$V + V_2O -> V_3$	$CC + I -> CCI*$
$I + B_S -> B_i$		$B_i + C_S -> BC$
		$B_i + O -> BO$
		$B_i + B_S -> BB$
Reactions in PKA region		
$I + V -> Si$	$V + V -> V_2$	
$I + I_N -> I_{N+1}$	$V + V_N -> V_{N+1}$	

*Not thought to be electrically active

The proportionality constant, α, known as the damage constant has the value $(5-10)\times 10^{-17} Acm^{-1}$ immediately after irradiation. α anneals exponentially after the end of irradiation with a series of time constants. These time constants are temperature dependent and at room temperature the current anneals by approximately 50 % over a period of 14 days, but unlike the depletion voltage no reverse annealing have been observed.

3.4.4 Radiation damage models

According to studies performed for LHC[15] there are three elementary defects formed during irradiation. These defects are vacancies(V), interstitials(I) and divacancies(V_2). Divacancies are static until about 600K while vacancies and interstitials are mobile except at very low temperatures. Some of the defects escape initial recombination and diffuse through the crystal reacting with other defects and impurity atoms like oxygen and carbon. The reaction rates are controlled by the concentration of impurities and their relative capture radii. The main reactions in this kinetics model are given in table 3.1. The subscripts i and S stands for interstitial and substitutional, respectively. Reactions B occurres during Primary Knock-on Atom cascades. The cluster forming of vacancies and interstitials may also occur for diffusing vacancies and interstitials after heavy neutron irradiation.

Chapter 4

Experimental setup

The measurements in this thesis can be divided into two types. The first measurements that are performed on detectors are typically CV- and IV-measurements. Single strip measurements are more time consuming than the first measurements and only detectors with good CV- and IV-characteristics are measured in this way. Since this thesis has been done i collaboration with both CERN and SINTEF, some measurements have been done at SINTEF and some at CERN. This makes it important to describe the different setups that have been used in the different locations.

4.1 CV and IV measurements

The capacitance and leakage current are important electrical properties of a silicon detector. High leakage current and high capacitance both increase the noise in the readout system. In addition will high leakage current increase the temperature in the detector, which, since the leakage current is temperature dependent, again increase the leakage current. After irradiation the leakage current is significantly higher than before irradiation, and the measurements have to be done at low temperatures to avoid thermal run-away. This is specially important when the area of the detector is large. The microstrip detectors have therefore been measured at $-18°C$, while the diodes have been measured at room temperature since the diodes total leakage current was at an acceptable level. Sections 3.1.2 and 3.2 describes the leakage current as proportional, and the capacitance as inverse proportional, to the

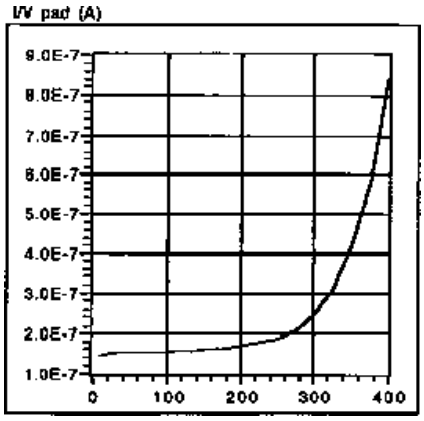

Figure 4.1: Current(A) vs. voltage(V) for a silicon detector

the width of the depletion region. The width of the depletion region, d, is given in equation 3.10 and depends on the square-root of the reverse bias, V_B. While the leakage current looks linear after full depletion, is it a function of $V_B^{1/2}$ before full depletion, this from the dependence on the depletion width. Similarly the capacitance is linear after full depletion, and a function of $V_B^{-1/2}$ before that limit. Examples of typical IV- and CV-measurements are shown in figure 4.1 and figure 4.2, respectively. IV- and CV-curves for an irradiated detector will have about the same shape as an unirradiated detectors, but with values that are functions of the fluence(sections 3.4.2 and 3.4.3). The measurement of capacitance is also used to calculate the full depletion voltage, or the operation voltage of the detector. This parameter is together with the leakage current the most used parameters when comparing different detectors. In the rest of this thesis it is therefore these two electrical properties of the detector that will be discussed in most detail.

The measurement setup is a standard setup at SINTEF. It is an automatic measurement system that first measures the capacitance as a function of reverse voltage, then ramps down the voltage and starts measurements of the current in active area and guard as a function of reverse voltage. The measurements are done with a LabVIEW program that both controls and reads out data from the instruments. The setup consist of a HP 4275 A LCR-meter, two Keithley 487pA-meter/V-source, a HP 3488A Scanner, a coupling box and a 24V voltage source. The two Keitleys are used for both biasing of the detector and for current measurements. The coupling box ties together the instruments and a relay connects the LCR-meter to the circuit for capacitance measurements. The voltage for the relay is delivered from the 24V

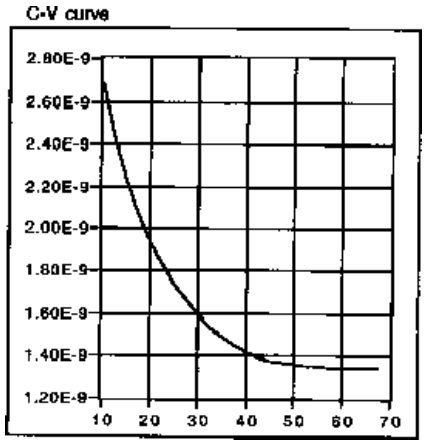

Figure 4.2: Capacitance(F) vs. voltage(V) for a silicon detector

voltage source. An equivalent scheme for the setup is seen in figure 4.3.

The setup at CERN is also an automatic measurement system like the one at SINTEF, but with only one measurement sequence instead of two. This LabVIEW program ramps up the voltage while it measures both capacitance and current. The setup consist of a HP4263B LCR-meter for capacitance measurements, and a Keithley 237 high voltage source measure unit for biasing the detector and measure current. The LCR-meter is not capable of delivering high voltages for CV-measurements, and the bias box is introduced in the circuit to provide this high voltage. A scheme for this setup can be seen in figure 4.4.

In addition to the instruments and the equipment used before irradiation a climate cabinet was needed for post-irradiation measurements. Pt100 elements was put in the cabinet to cross-check the cabinets temperature control. At SINTEF a single two-wire Pt100 element was connected to a Fluke Hydra-multimeter. The Pt100 element was then attached to a large aluminium chuck that was made large enough to keep an approximately constant temperature even when the door was opened to take out or put in diodes. When the diodes were put into the chamber they were put on the chuck so that the diodes quickly would obtain the cabinets temperature. At CERN two four-wire Pt100 elements were connected to a Keithley2001 measurement unit. These Pt100s were put in the bags of two detectors, one in the front and one in the back of the cabinet, to check the temperature uniformity of the cabinet. thirteen detectors with aluminium framing have a large thermal mass and were therefore slower to cool down than the cabi-

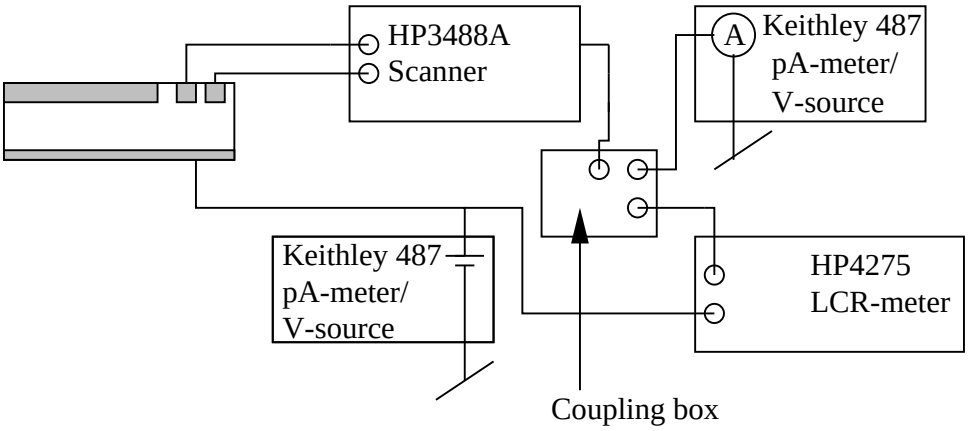

Figure 4.3: Equivalent scheme for the setup at SINTEF

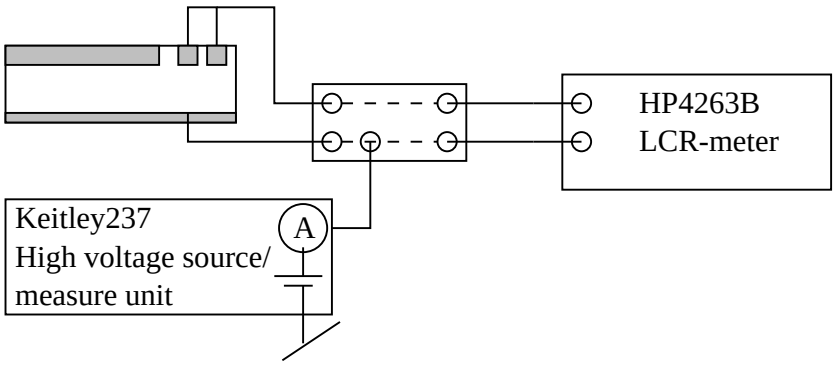

Figure 4.4: Equivalent scheme for the setup at CERN

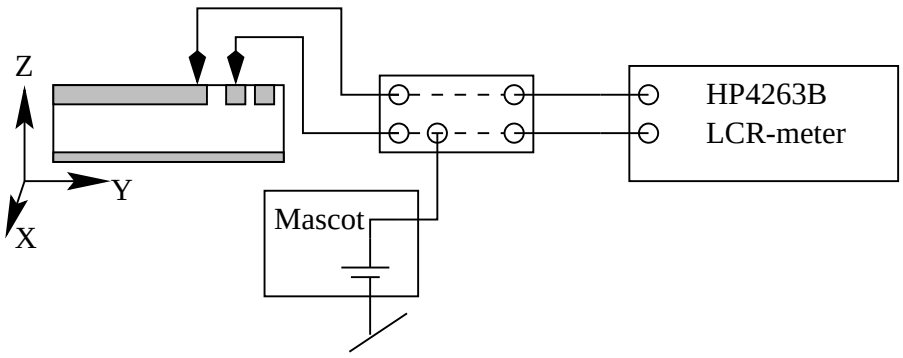

Figure 4.5: Scheme for single strip measurements

net. The PT100 measurements made it possible to decide when the detectors temperature reached $-18°C$, and therefore when to start the measurements.

4.2 Single strip measurements

Microstrip detectors may have defects like broken strips, shorted strips and holes in the oxide. A perfect detector has no strip defects, but the processing of very thin lines makes this difficult to achieve. Broken- and shorted strips are defects that depends on the processing only, and the number of these effects are not expected to increase when the detectors are irradiated. One effect of irradiation is the introduction of charge in the oxide, and this can introduce oxide punch-troughs at sufficient high voltages. The number of pinholes are therefore expected to increase during irradiation. Defect strips decrease the position resolution and increase the noise, and it is therefore important to use devices that have few defects. The ATLAS specifications, before and after irradiation, are a mean acceptance of 99% with no devises below 98%, or less than 7 and 15 bad strips, respectively.

At SINTEF these measurements are done together with the measurements of the coupling capacitance. This setup consist of a HP4263B LCR-meter, a Mascot 12V voltage source, a bias box and a xyz-stage controlled with a Owis microstep motor driver. A scheme for this setup can be seen in figure 4.5. The motor driver and the CV-meter is controlled with a LabVIEW program in such a way that after a measurement on one strip the stage moves to the next strip for a new measurement.

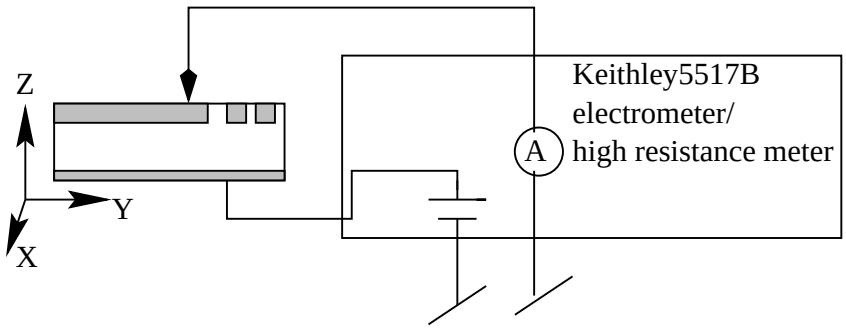

Figure 4.6: Setup for measurements of pinholes in a microstrip detector

Another method to find strip defects is to combine capacitance- and current-measurement on each strip. With this method the capacitance and current are measured between each strip and the backside. The current measurements are done to find holes in the oxide while the capacitance measurements finds shorts and breaks. In this thesis only current measurements has been done in this way, and a scheme for the current measurement setup is given in figure 4.6.

Chapter 5

Measurements on diodes

From the previous chapter it is easy to see that for silicon detectors there are three important parameters, the leakage current, the depletion voltage and strip integrity. In an annealing study of ATLAS microstrip detectors [11] one SINTEF p-in-n detector was found to have significantly lower depletion voltage than the rest of the detectors in the study. SINTEF had two hypotheses to explain this phenomenon, one was that their gettering process and the second was the phosphorous concentration on the back side. The gettering is a temperature treatment of the detector that removes different impurities from the silicon. These impurities are trapped in the phosphorous, and it has been shown that a high phosphorous concentration increases the solubility of some impurities. Section 3.4.4 show that the depletion voltage depends on radiation induced defects that reacts with initial impurities in the silicon substrate. The phosphorous concentration and the gettering changes the initial impurity concentration, and it is therefore possible that changes in the phosphorous concentration and/or the length of the gettering can change the depletion voltage.

Simple pn-junction diodes have the same basic properties as the active area of a micro strip detector, but the diodes have no strips and are therefore easier to process. This, and the fact that you can produce more than one diode per wafer, makes diodes cheaper than the micro strip detector. Diodes are therefore very suitable for experiments on different processing parameters. Since the diodes do not have strips only leakage current and depletion voltage will be considered in this chapter.

The diodes used in this experiment are listed in table 5.1. The gettering is

Table 5.1: Information on diodes in test

Diode	*Gettering*	*Phosphorous concentration*
1d1, 1d2	No	P on entire backside, N_d unknown
2d1, 2d2	Short	P on entire backside, N_d unknown
3d1, 3d2	No	P in strips on backside, N_d unknown
4d1, 4d2	Short	P in strips on backside, N_d unknown
5d2	Short	3e10
6d1, 6d2	Long	3e10
7d3, 7d5	Short	1.6e12
8d3, 8d5	Long	1.6e12
9d3, 9d5	Short	2.5e12
10d3, 10d5	Long	2.5e12
11d1, 11d2	Short	1e15
12d1, 12d2	Long	1e15
13d1, 13d2	Short	5e15
14d1, 14d2	Long	5e15

a process that removes impurities from the active area to intentional trapping areas in the device. The diodes have been divided into three categories, short, long and no gettering. The diodes that received short gettering got 2 h at $800°C$ plus 2h at $600°C$, the ones that received long gettering got 20 h at $800°C$ plus 20h at $600°C$. All the diodes are produced at SINTEF. Diodes 5d, 6d, 7d, 8d, 9d, and 10d are circular diodes with a diameter of $2.5mm$. The rest of the diodes are quadratic with area $1cm^2$.

5.1 Diodes before irradiation

CV-measurements were performed with reverse biasing from 2 to 200 volts. The frequency of the CV-meter was $10kHz$. Leakage current measurements were done with reverse biasing from 20 to 300 volts. The current measurements was limited to $1mA$ except from some of the first measurements when the limit was about $1\mu A$. The reason for this measurement limit is to protect the voltage source from overheating because of high current.

Capacitance measurements are a tool to find the necessary operating voltage of the detector, but the best method is CCE measurements. The detector is connected to read-out electronics when CCE measurements are done. A

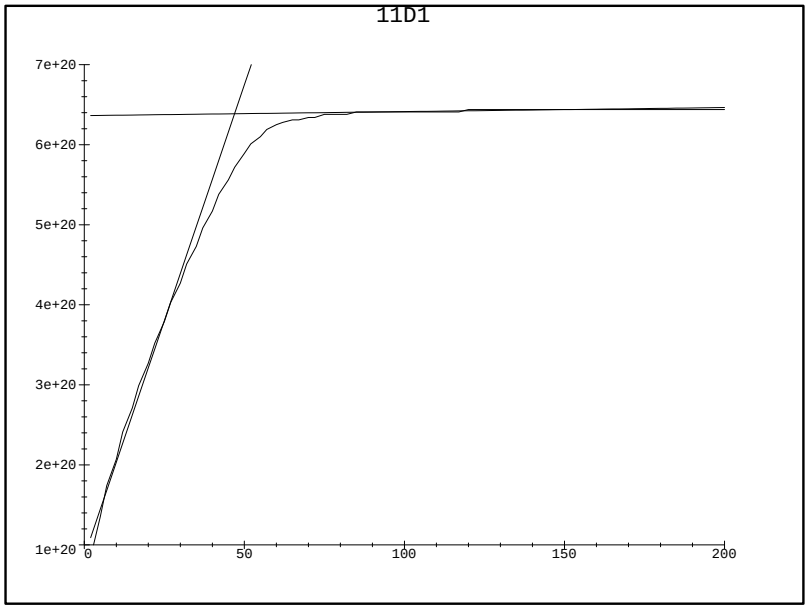

Figure 5.1: Finding the depletion voltage from the crossing of two lines fitted to a plot of $1/C^2(F^{-2})$ vs. reverse bias voltage(V).

particle source injects particles in the detector and produces charge carriers that are read out with the electronics. The CCE is usually measured as the S/N-ratio as a function of voltage, so Charge Collection Efficiency is a somewhat misleading name. The CCE increases with applied reverse voltage until the depletion voltage where a plateau is reached. Capacitance measurements are easier to perform and for unirradiated detectors give results that are close to the CCE measurements. After irradiation however, the capacitance of a detector depends on frequency and temperature[4], and it follows that the depletion voltage found with these methods is temperature and frequency dependent. Clearly, CCE measurement is a better method to find the best estimate of an irradiated detectors depletion voltage. The depletion voltage found from CCE measurements is usually higher than the values found from CV- measurements, but the CV-measurements can still be used to compare different detectors. In this experiment the depletion voltage was found from the crossing of two straight lines fitted in a $1/C^2$ plot as shown in figure 5.1. The depletion voltage and leakage current of all the diodes are given in table 5.2. A problem with the measurements was the leakage current. Some of the diodes had soft breakdowns at rather low voltages. A simplified de-

scription of a LCR-meter will explain why this is problem. A LCR-meter applies a small voltage to the diode and then measures the current over the diode. The meter then calculates the capacitance from the current and the applied voltages frequency and amplitude. The capacitance can be written as dQ/dV_R, and since a soft breakdown increases the current gradient and therefore also the calculated charge gradient, the soft breakdown does increase the capacitance. This effect can give a U-shaped C vs. V curve that makes it impossible to find the depletion voltage with the $1/C^2$ method. Depletion voltages that could not be found because of breakdowns are marked with B's in the table.

5.2 Diodes after irradiation

The diodes were irradiated unbiased to a fluence of 2×10^{14}neutrons/cm^2, which should be about equal to 3.3×10^{14}protons/cm^2[5]. The irradiation lasted for 17 minutes and 30 seconds and was done at the Josef Stefan institute in Lubljana, Slovenia. After the irradiation the diodes were marked and put in plastic bags, then kept cold and transported to Oslo. The diodes were then again stored in a freezer to reduce any kind of annealing.

CV-measurements were performed with reverse biasing up to 400 volts and the same measurement frequency as used before irradiation. The leakage current measurements were made in the same way as before irradiation. ATLAS is to be operated at $-7°C$ with a yearly maintenance period when the temperature will be $20°C$ for two days and $17°C$ for two weeks. From [6] there are two different annealing stages, one centered about 370K and the other about 440K. The 370K stage is the one responsible for reverse annealing at room temperature and the temperature has been kept under this level to avoid interference from the second stage. The reverse annealing was accelerated by keeping the diodes at $\approx 60°C$, and an accumulated annealing time of 460 minutes should simulate the ATLAS scenario[9]. There were 11 warm up steps, two times 5 minutes, two times 10 minutes, 20 minutes, 5 times 60 minutes and in the end 110 minutes, to a total of 460 minutes. Before and after each step measurements were done at room temperature, and the diodes were put back in the freezer when there were pauses in the measurements. The room temperature was measured approximately with an ordinary thermometer and taken into account when normalizing the annealing time. The temperature dependence of the reverse annealing is given in equation 3.20 and from this can the annealing at a temperature T_2 be

Table 5.2: Pre-Irradiation measurements of diodes

Diode	Leakage current at $100V(A)$	Leakage current at $200V(A)$	Leakage current at V_{dep}	Depletion voltage(V)
1d1	1.50E-04	>1.00E-03	>1.00E-03	B
1d2	2.00E-06	>1.00E-03	>1.00E-03	43.7
2d1	4.10E-05	>1.00E-03	>1.00E-03	B
2d2	1.40E-04	>1.00E-03	1.20E-07	B
3d1	4.40E-08	5.00E-08	2.70E-08	40.1
3d2	3.80E-08	4.80E-08	3.10E-08	39.6
4d1	7.50E-06	>1.00E-03	6.00E-09	B
4d2	6.10E-09	1.00E-06	5.00E-09	43.8
5d2	3.90E-08	3.00E-07	1.50E-09	17.6
5d3	6.40E-08	4.30E-07	2.00E-09	16.6
6d1	3.60E-08	3.40E-07	4.00E-10	19.0
6d2	7.80E-08	8.00E-07	5.00E-10	20.0
7d3	5.00E-10	1.40E-09	1.80E-10	20.7
7d5	4.90E-10	1.30E-09	1.60E-10	24.3
8d3	1.10E-10	3.40E-10	5.00E-11	25.5
8d5	1.20E-10	3.70E-10	5.50E-11	21.7
9d3	2.30E-10	6.70E-10	5.50E-11	30.2
9d5	2.70E-10	5.40E-10	5.50E-11	27.5
10d3	1.30E-10	3.80E-10	6.50E-11	32.7
10d5	1.10E-10	2.60E-10	3.80E-11	27.2
11d1	2.50E-09	5.10E-09	1.80E-09	43.5
11d2	2.70E-09	3.30E-09	2.00E-09	39.8
12d1	2.90E-09	4.70E-09	2.00E-09	36.0
12d2	2.70E-09	5.50E-08	2.00E-09	37.9
13d1	4.90E-09	3.30E-08	1.80E-09	41.3
13d2	2.50E-09	2.00E-08	1.90E-09	39.6
14d1	4.80E-09	7.80E-09	1.90E-09	44.9
14d2	2.30E-09	1.30E-07	1.70E-09	42.4

normalized to a temperature T_1 with the relation:

$$\frac{1}{\tau_L(T_2)} = \frac{x(days)}{\tau_L(T_1)} \tag{5.1}$$

The 10 year ATLAS scenario compares to 21 days at $25°C$ with this relation. This relation was used to normalize the annealing time of the $60°C$ measurements to $25°C$, and the calculated total annealing time was about 60 days. With this normalization the full depletion voltage reached its minimum value after about 15 days. Earlier experiments have shown that this normally occurs after 5-7 days, and indicates that this normalization is not very good when dealing with high temperatures.

5.2.1 Leakage current

Problems with the LabView program limited this overview of leakage current to the currents at $100V$ and $200V$. The leakage current is temperature dependent and from equation 3.1 was normalized to $T_1 = 20°C$ with this relation:

$$I_{T_1} = I_{T_2} \left(\frac{T_1}{T_2}\right)^{3/2} exp\left(\frac{E_g}{2k}\left(\frac{1}{T_2} - \frac{1}{T_1}\right)\right) \tag{5.2}$$

Figure 5.2 and figure 5.3 give an overview of the currents of all diodes at $100V$ and $200V$. As can be seen from this figure the smaller diodes have larger leakage current per cm^2 than the larger ones. This makes it more difficult to compare differences due to process parameters than it would have been if all the diodes had the same size. Separate figures of small and large diodes have therefore been made to ease this comparison. The currents for each pair of small diodes can be seen in figure 5.4 for $100V$ and figure 5.5 for $200V$. Similar plots of the current in the larger diodes are shown in figure 5.6 and figure 5.7.

5.2.2 Depletion voltage

Different methods have been used in previous experiments to find the depletion voltage and in this thesis two methods have been used. The first uses the crossing point of one straight line with a fixed level at C_0, the capacitance measured before irradiation. The limitation of this method is that you need to know the correct capacitance. For the smaller samples in this

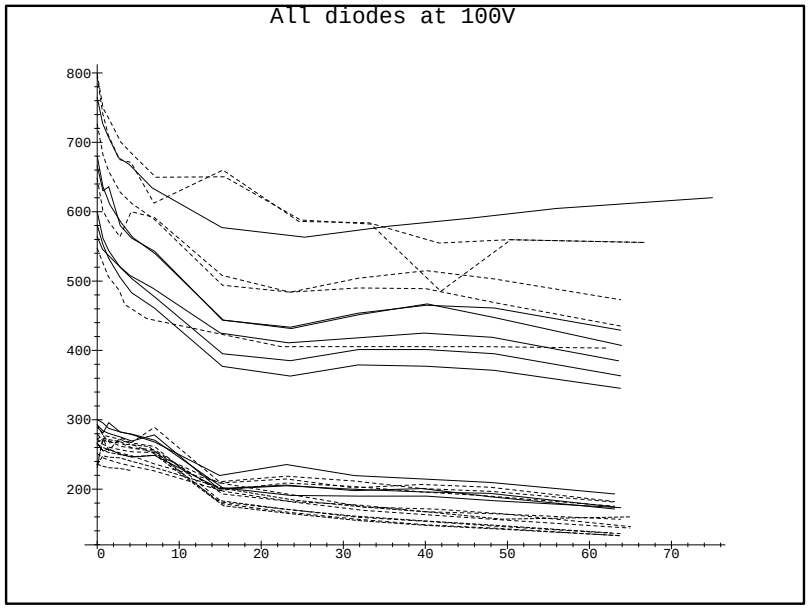

Figure 5.2: Current($\mu A/cm^2$) vs. time(days) at $100V$. The stippled lines represents the diodes that received the shortest gettering.

experiment stray capacitance was a problem and when applying this method strange results occurred. The second method is the same method that was used for unirradiated diodes. The depletion voltage does not depend on C_0, but there is another important limitation with this method. To find the plateau of constant capacitance reverse biasing to much higher values than the depletion voltage is needed. From equation 3.18 and equation 3.23 the initial depletion voltage is about $350V$. Since the setup has a limitation on $400V$ this made it difficult to find the depletion voltage in the beginning and end of the annealing, where the depletion voltage is at its highest. Some diodes had so high depletion voltage that they could not be measured with this method. The smaller diodes had problems with soft breakdowns at high voltages and it was, as explained in the previous chapter, impossible to find the depletion voltage. As can be seen in figure 5.8 there were a difference in the depletion voltages found with the different methods. Since both methods gave troubles with the smaller diodes these have been left out of this overview. Method one had also problems with 1D1, 2D1, 2D2 and 3D2 since C_0 is unknown for these diodes. For this reason the results are presented in figure 5.9 found as with the $1/C^2$-method.

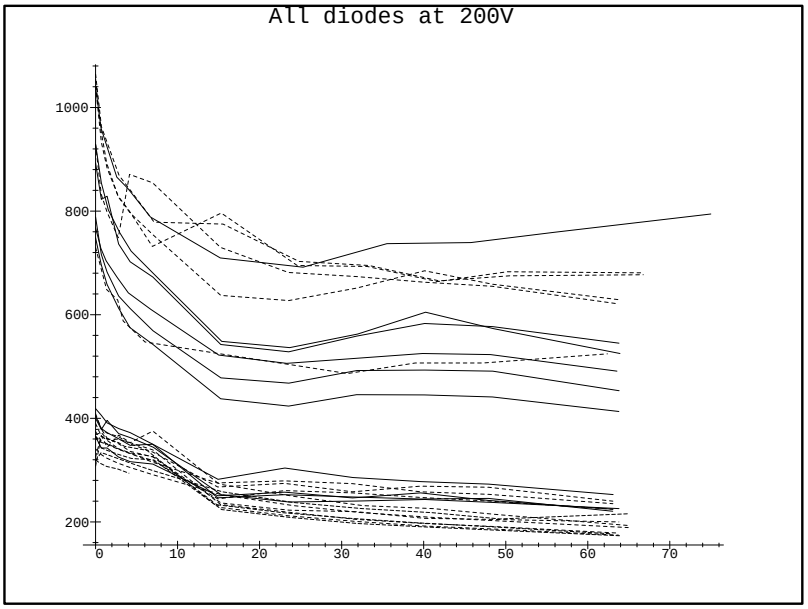

Figure 5.3: Current($\mu A/cm^2$) vs. time(days) at $200V$. The stippled lines represents the diodes that received the shortest gettering.

5.3 Summary

The measurements in this section were done to examine a possible correlation between processing parameters and electrical performance after irradiation for silicon pn-junction diodes. This section is a short summary of the results and the limitations of these measurements. A preliminary conclusion will be drawn at the end of this section, but a more thorough discussion taking into account the detector results, is given in section 7.

This experiment was designed to find out whether the processing of a detector influence the full depletion voltage after irradiation. Since the experiment was mainly concerned with the full depletion voltage, the leakage current was not considered to be that important for the study. It was therefore not put much weight on the details of how the leakage current measurements should be done. Later, this has proven to be a limitation of the study. The full depletion voltage has been found with the use of two different methods described in section 5.2.2. That section also describes the limitations of these methods, and explains why some of the diodes had to be left out of this

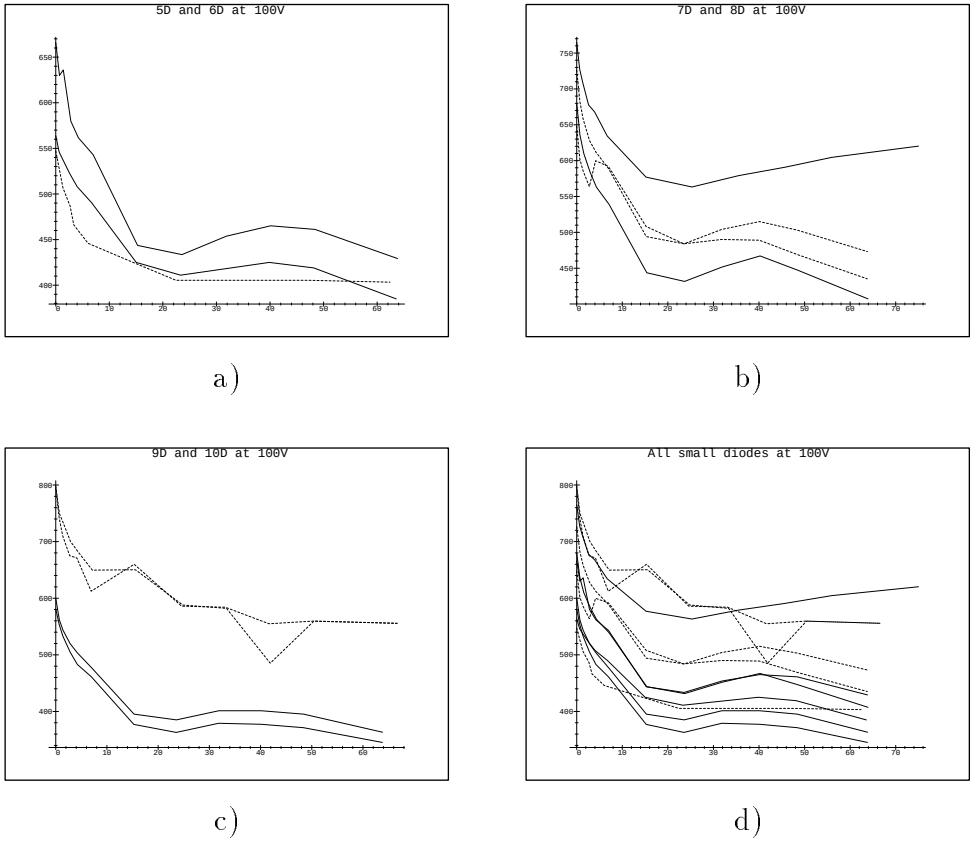

Figure 5.4: Current($\mu A/cm^2$) vs. time(days) at $100V$. The stippled lines represents the diodes that received the shortest gettering.

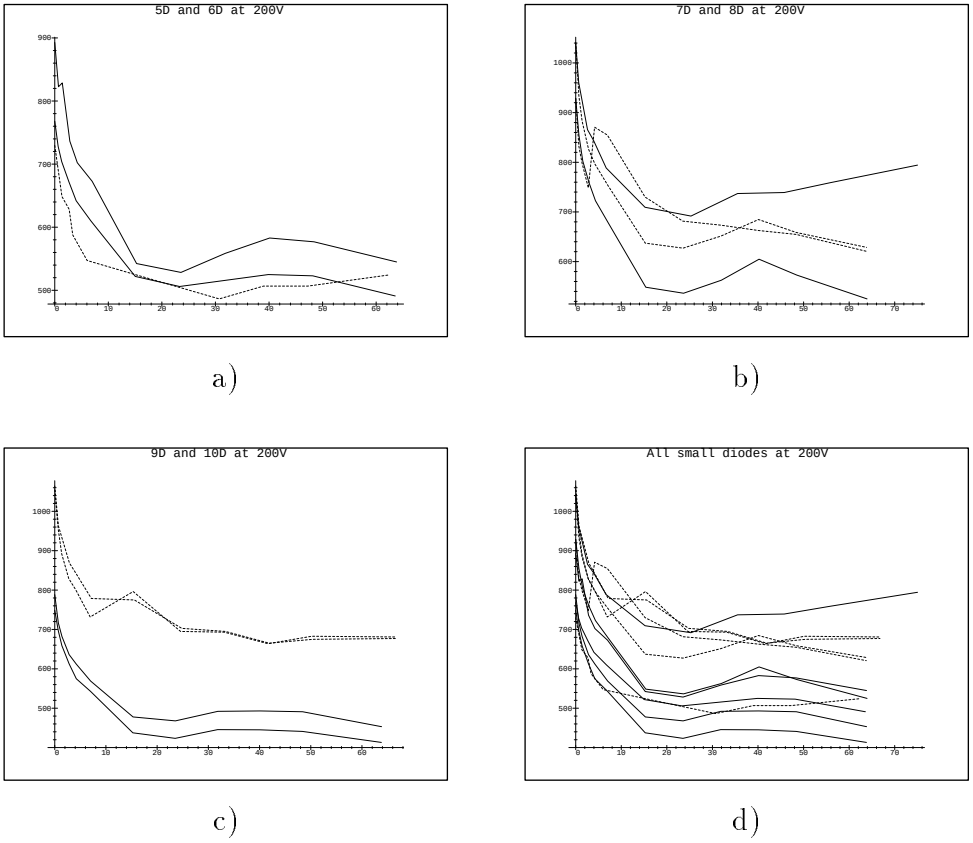

Figure 5.5: Current($\mu A/cm^2$) vs. time(days) at $200V$. The stippled lines represents the diodes that received the shortest gettering.

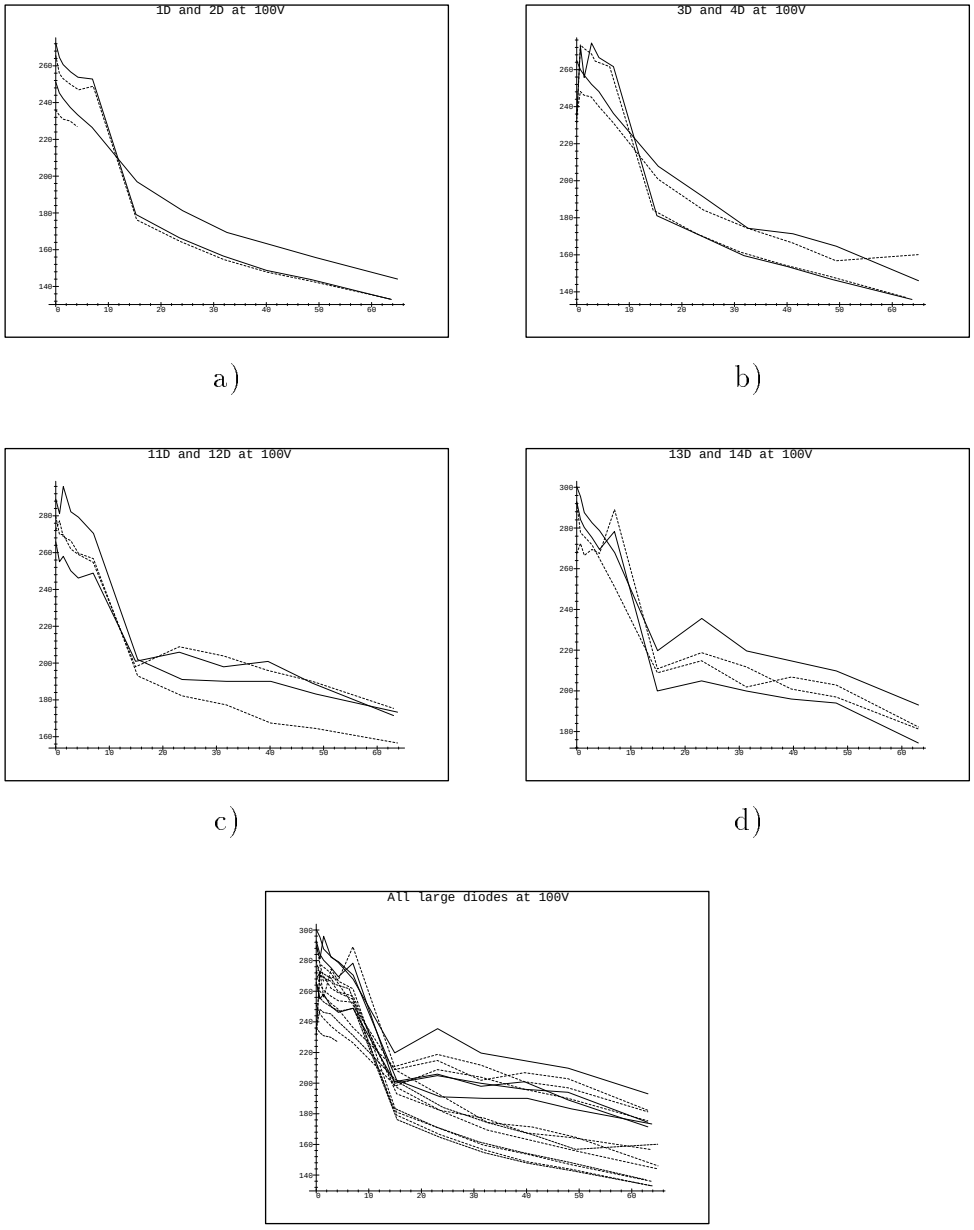

Figure 5.6: Current($\mu A/cm^2$) vs. time(days) at $100V$. The stippled lines represents the diodes that received the shortest gettering.

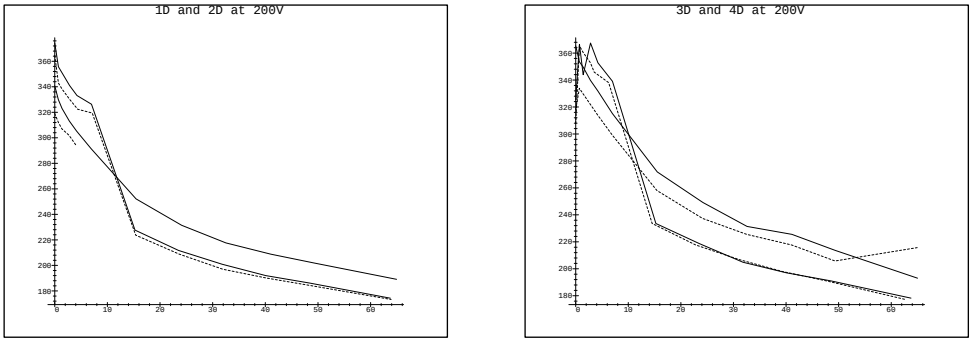

a)

b)

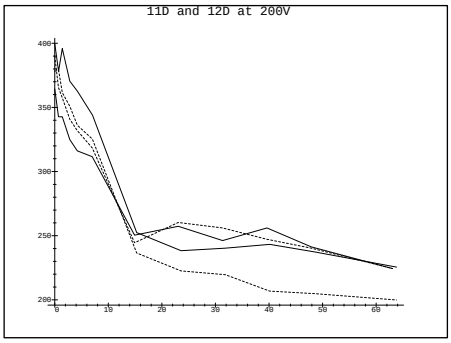

c)

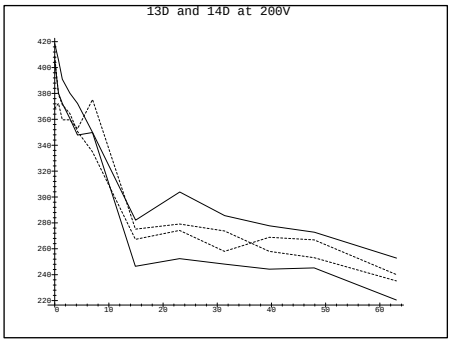

d)

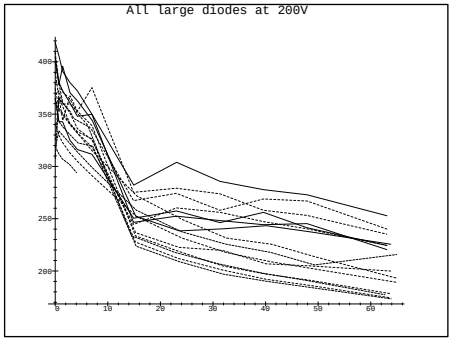

e)

Figure 5.7: Current($\mu A/cm^2$) vs. time(days) at $200V$. The stippled lines represents the diodes that received the shortest gettering.

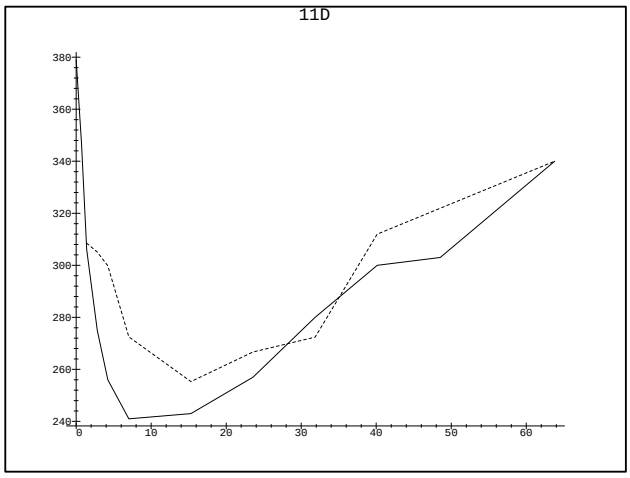

Figure 5.8: V_{dep} vs. $Time$ for 11D1. The difference between the two methods described in the text, can easily be seen.

analysis. On the other hand it was possible to do leakage current measurements for all diodes. These measurements have therefore been more valuable to this study than first thought, and of this reason the limited planning of current measurements has degraded the outcome of the study. At least one important parameters should have been changed in the design of the current measurements, namely the maximum reverse voltage. An increase in maximum reverse voltage up to the software limit of $400V$ would have enabled a study of soft breakdown in the irradiated diodes.

One thing that comes to mind when the data from the current and the depletion voltage measurements are studied, is that the spread in values for identical diodes are on the same order of magnitude as the spread for the non-identical ones. In addition there are an overlap between these sets of data. In other words there are no systematic difference between diodes that are processed differently, and this indicates that both the full depletion voltage and the leakage current are independent of the processing parameters studied in this thesis. It is therefore interesting to compare diodes 9D and 10D. This set of diodes shows a significantly lower leakage current for the diodes that received the longest gettering, and thus indicates that the leakage current does depend on the length of the gettering. These two results put together leads to the conclusion that the length of the gettering can be important for the radiation hardness of a detector if the detector have some given initial

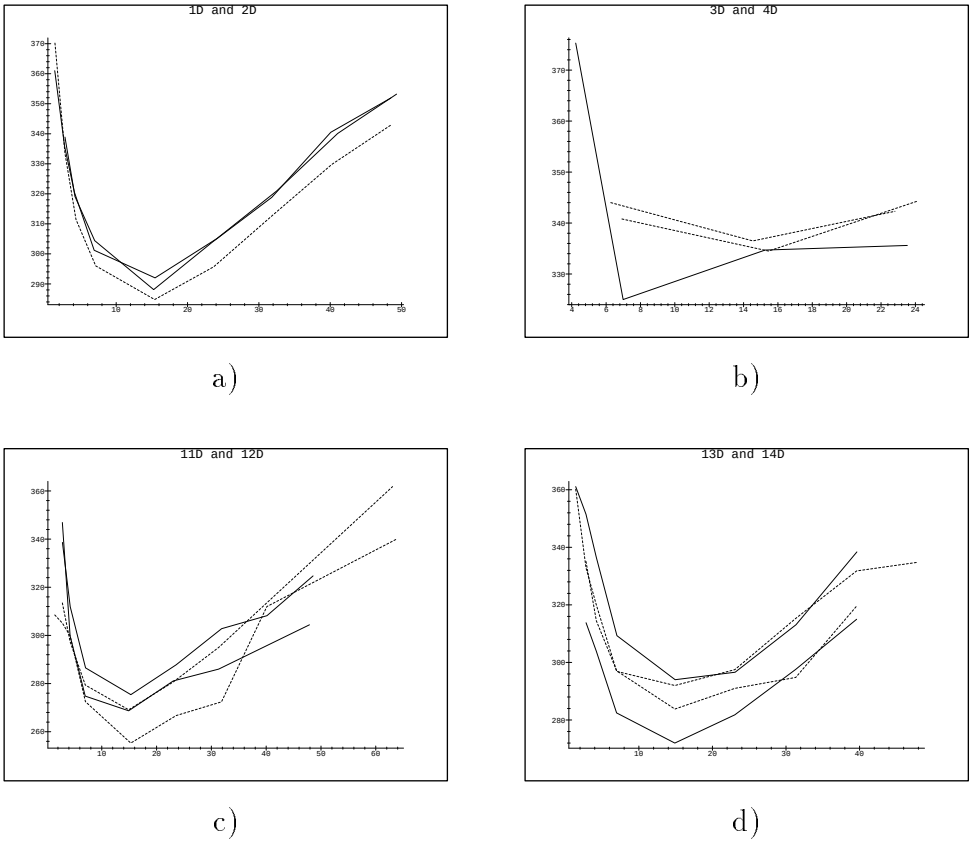

Figure 5.9: V_{dep} vs. time(days) for all large diodes. The stippled lines represents which of the diodes that received the shortest gettering.

properties.

Chapter 6

Measurements on detectors

Detectors with different process parameters were made to continue the study on the diodes. These parameters are given in table 6.1. Irradiation capacity problems at CERN limited the study to only 10 detectors. The irradiation run was part of the detector qualification for the ATLAS project, and explains why most of the detectors in this study are standard detectors, in the range 21-50.

6.1 Detectors before irradiation

CV-measurements were performed with reverse biasing from 10 to a maximum of 80 volts. The reason for a non-constant maximum voltage was that the program was set to calculate the depletion voltage and then stop the measurements at a certain level above that voltage. The frequency of the CV-meter was $10kHz$. Leakage current measurements were done with reverse biasing from 20 to 400 volts. The current measurements were limited to $25\mu A$ to protect the voltage source from overheating because of high current. The single strip measurements were done with a frequency of 100Hz and a $400mV$ AC-level.

As for the diodes the depletion voltage was found from the crossing of two straight lines fitted in an $1/C^2$ plot. The different strip defects are found from coupling capacitance measurements, and in figure 6.1 all three types of defects can be seen.A broken strip gives an infinite capacitance, in practice the maximum capacitance of the meter. The shorted strips have coupling ca-

Table 6.1: Information on detectors in test

Detector	*Thickness*	*Orientation*	*Restivity* ($k\Omega$)	*Edge contact*	*Process variation*
1-5	300	$< 100 >$	6-9	No	Extra large phosphorus concentration
6-10	300	$< 100 >$	6-9	No	Very low phosphorus concentration
11-15	300	$< 100 >$	6-9	No	Low phosphorus concentration, Short gettering
16-20	300	$< 100 >$	6-9	No	Short gettering
21-30	300	$< 100 >$	6-9	No	
31-50	300	$< 100 >$	6-9	Yes	
51-60	280	$< 111 >$	3-6	No	
61-70	280	$< 111 >$	3-6	Yes	
71-75	300	$< 111 >$	1.2-3	Yes	

pacitances that have a linear relation to the number of strips that are shorted. Two shorted strips doubles and three strips triples the coupling capacitance. This is because two shorted strips have effectively twice the area of one strip and therefore twice the capacitance. Broken strips can be seen from values lower than the mean value. This is the opposite effect of the shorted strips since broken strips have smaller area and therefore lower capacitance. The results of the two measurements are given in table 6.2 and table 6.3. An alternative method to find strip defects is described in section 4.2 and some measurements were done with this method to find pinholes. This alternative method is to measure the current between each strip and the backside. The ATLAS SCT community has defined that a strip has a pinhole if the strip current exceeds $2pA$ at $100V$ reverse bias. The number of pinholes found from both methods are summarized in table 6.4.

6.2 Detectors after irradiation

The detectors were irradiated at $100V$ reverse bias to a fluence of 3.0×10^{14} protons/cm^2. The irradiation was done at the PS at CERN and lasted for

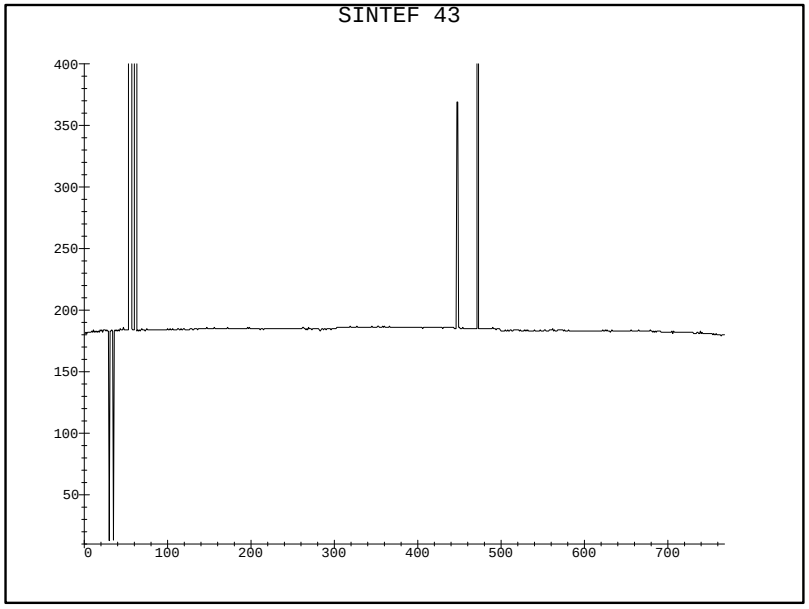

Figure 6.1: Single strip measurements

Table 6.2: Pre-Irradiation measurements on detectors

Detector	*Leakage current(A) 150V*	*Leakage current(A) 350V*	*Depletion(V) Voltage*
10	4.30E-07	8.00E-06	46.0
12	4.90E-07	1.20E-06	51.7
22	5.20E-07	2.30E-06	40.5
27	8.80E-07	9.70E-07	48.5
28	1.70E-07	2.90E-07	45.0
29	2.40E-07	7.50E-06	46.0
36	4.10E-07	9.00E-07	47.0
39	4.60E-07	5.70E-07	42.7
45	1.60E-07	4.00E-07	42.4
48	2.30E-07	7.30E-07	47.4

Table 6.3: Strip quality before irradiation

Detector	*Pin-holes*	*Shorted Strips*	*Broken strips*
10	1	0	0
12	0	0	0
22	0	0	0
27	1	0	0
28	0	0	0
29	1	2	0
36	0	0	0
39	0	0	0
45	0	0	1
48	1	0	0

Table 6.4: Pinholes before irradiation found from coupling capacitance measurements(method 1) and current measurements(method 2).

Detector	*Method 1*	*Method 2*
9	3	23
11	0	5
20	1	10
31	1	3

approximately one week. After the irradiation the detectors were put in plastic bags and put in a freezer. A bag containing silica gel was added in each plastic bag to absorb moisture when cooling the detectors. Detector 28 was not irradiated during the same run as the rest of the detectors, but was irradiated about two months earlier. Some problems occurred during that run and it is not certain whether this detector received the same fluence as the rest of the detectors.

Eight of the ten detectors in the study were, as mentioned earlier, part of a qualification process and this put some limitations on the measurements. To get comparable results it was decided that all of the 49 detectors participating in the study should be measured in the same way. The measurements that had to be done to qualify were current and capacitance versus voltage up to 500V. These measurement were to be taken before annealing and at the minimum depletion voltage at $-18°C$. The ideal measurement would have been to put one detector in the climate cabinet to anneal while doing IV- and CV-measurements at suitable time intervals, but the large number of detectors made this approach too time consuming and another approach had to be used. Cables were made so that up to 13 detectors could be cooled down and measured at one time. After all 49 detectors had been measured all of them were put in the climate cabinet again for annealing. Earlier studies have shown that minimum depletion voltage occur about 7 days after the start of annealing at $25°C$[11][10], so the detectors were put back in the freezer after 4.4 days of annealing at $28°C$(equation 5.1). Measurements were then done with the same measurement procedure as before annealing.

Table 6.4 show that more pinholes are found from the current measurements at $100V$ than the coupling capacitance measurements. Measurements on oxide punch-troughs have therefore been done with this method. The pre-irradiation measurements was done with the first less efficient method, and this might have made the number of irradiation induced pinholes, table 6.5, artificially high. It should also be noted that the detectors were bonded during measurements. Short-circuits caused by the bonding wires may have increased the number of pinholes to some level. The numbers in parenthesis is the number of pinholes if those shorts are subtracted.

Table 6.5: Pinholes before and after irradiation

Detector	*Before irradiation*	*After irradiation*	*Irradiation induced pinholes*
10	1	12	11
12	0	10(8)	10(8)
22	0	6	6
27	1	13(9)	12(8)
28	0	0	0
29	1	6	5
36	0	0	0
39	0	0	0
45	0	4	4
48	1	6	5

6.2.1 Leakage current

The leakage current can be summarized in two tables. Table 6.6 shows the current in both guard and active area before annealing, while table 6.7 shows the current after 4.4 days of annealing.

6.2.2 Depletion voltage

The setup used for current and capacitance measurements was not optimal for capacitance measurements. The interesting part of the detector for both capacitance- and CCE-measurements is the active area of the detector, and measurements should therefore be done over that area only. In this setup the active area is connected to the guard structure, and strange behaviour have been observed because of this. Figure 6.2 and figure 6.3 show $1/C^2$ plots for all ten detectors before and after annealing, respectively. Normally is the capacitance flattening out at full depletion, but when the guard was connected different behaviours were observed at about this voltage. One behaviour was that the capacitance started to decrease again, and then later stabilize at another lower level, see figure 6.2b). Figure 6.2f) shows another behaviour, an instability in capacitance. The electric fields in a inverted detector are not as well understood as in an un-irradiated detector and it is therefore difficult to explain this. On some detectors it looks like the

Table 6.6: Leakage current before annealing. Measurements done at $-18°C$.

Detector	*Leakage current 160V (μA)*	*Leakage current 360V (μA)*
10	212	263
12	193	239
22	214	273
27	197	246
28	174	212
29	204	248
36	204	258
39	201	250
45	216	231
48	197	254

Table 6.7: Leakage current after 4.4 days at $28°C$. Measurements done at $-18°C$.

Detector	*Leakage current 160V (μA)*	*Leakage current 360V (μA)*	*Leakage current 500V (μA)*
10	149	167	182
12	150	169	182
22	143	162	178
27	142	158	172
28	132	147	158
29	146	164	181
36	145	165	217
39	139	157	201
45	133	148	162
48	138	153	164

Table 6.8: Depletion voltage of all ten detectors. Measurements done at $-18°C$.

Detector	*Depletion voltage(V)*	
	Before annealing	*Annealed 4.4 days at 28°C*
10	225	129
12	240	147
22	250	151
27	240	148
28	200	158
29	200	123
36	200	112
39	200	120
45	250	128
48	250	148

unstable behaviour is superposed on the lower capacitance level. This makes an unstable guard ring a probable reason. The unstable behaviour made it difficult to calculate the depletion voltage, so the values before annealing in table 6.8 are very approximate. Before the next measurements the unstable behaviour, to some level, had annealed out. It was therefore much easier to calculate the depletion voltage and the values in the table should be correct.

6.3 Summary

The measurements in this section were done to examine a possible correlation between processing parameters and electrical performance after irradiation for silicon microstrip detectors. This section is a short summary of the results and the limitations of these measurements. A preliminary conclusion will be drawn at the end of this section, but a more thorough discussion taking into account the diode results, is given in section 7.

The limitations of the detector measurements are all due to the fact that the detectors was part of the ATLAS detector qualification process. This put limitations on both the experimental setup and the selection of detectors that

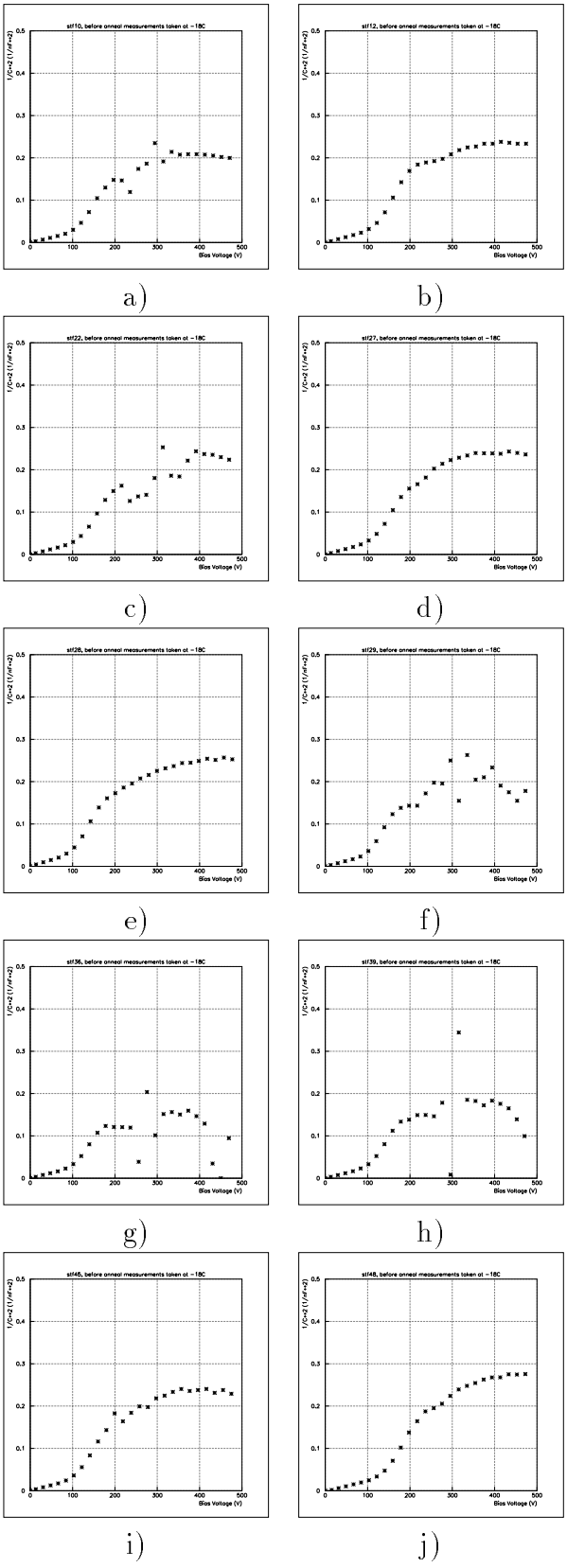

Figure 6.2: $1/C^2$ for all detectors before annealing

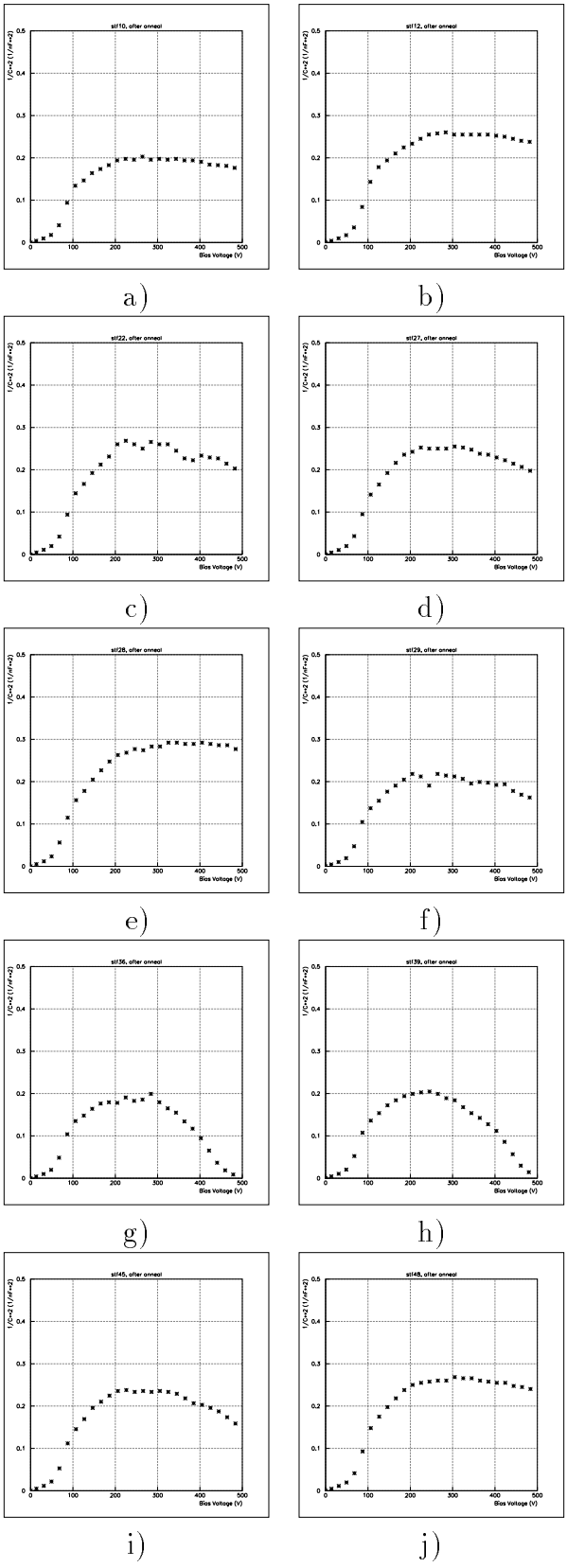

Figure 6.3: $1/C^2$ for all detectors after annealing

participated in the study. The limitations on the experimental setup resulted in only two measurements on each detector, and capacitance measurements that were difficult to interpret. These limitations are described in more detail in section 6.2, but the fact that eight out of ten detectors in the study were standard detectors made it possible to see the spread in leakage current and depletion voltage for identical diodes. The limited number of detectors with experimental processing parameters made it difficult to find any differences from the standard detectors.

There was as expected an increase in pinholes for some detectors, table 6.5, but no correlation was observed between the number of pinholes before and after irradiation. The tables of leakage currents after irradiation, table 6.7 and table 6.6, show that no significant difference in leakage current can be observed for any of the detectors, except for detector 28. Detector 28 was irradiated in an earlier irradiation and the lower leakage current can be explained with a lower obtained fluence. The detector was also stored for some time, and annealing of the detector in that time can be another explanation of the low leakage current. Similar, the measurements of the full depletion voltage reveals no relation between the full depletion voltage and the different processing parameters, or between the full depletion before and after irradiation. These results leads to the conclusion that it is difficult to foresee the electrical performance of an irradiated detector based on the detectors pre-irradiation behaviour. Furthermore it can be concluded that the different processing parameters in this study did not influence the radiation hardness of the detectors under study.

Chapter 7

Discussion and conclusion

This thesis addresses two main topics. Subject number one was to find out if the processing parameters can alter the electrical properties of the detector after heavy irradiation. This study has been done by comparing leakage current and depletion voltage for detectors with different processing parameters. Subject number two was to find out if it is possible from the pre-irradiation measurements to foresee how the electrical performance of a detector will be after irradiation. If possible, this would be a tremendous advantage since it will be impossible to replace the micro strip detectors during the 10 years of ATLAS operation and good detectors have to be chosen from the beginning. To examine this subject comparisons of leakage current and depletion voltage before and after irradiation have been made.

7.1 Time normalization

The normalization of time to temperature is also subject to discussion. The time has been normalized with equation 5.1 that only takes τ_L, the long term annealing time constant, into account. From figure 5.9 it is possible to approximately find t_{min}, the time minimum depletion occur. When comparing this value of 14-16 days with the theoretical value of 4 days at $25°C$, you find a difference of 250-300%. This normalization has been used in other experiments too[11], and they found t_{min} to be about 7 days at the same temperature. This value is also about 100% wrong compared to theory, but the t_{min} of 7 days was still used as the correct value in the experiment de-

Table 7.1: Pre-Irradiation measurements on detectors

Fluence	V_{dep0}	V_{depMin}
3.0×10^{14}	720	318
3.3×10^{14}	792	350

scribed in chapter 6. The correct time dependence of V_{Dep} is not important for the results of this thesis, and no attempt has therefore been made to find a better normalization.

7.2 Depletion voltage

The full depletion voltage can be calculated from equation 3.18, and table 7.1 gives the theoretical values of the depletion voltage at minimum and immediately after irradiation. The minimum depletion voltage of the diodes have been plotted in figure 7.1 as a function of the pre-irradiation measurements. Figure 7.2 is a similar plot for the detectors. The values obtained by experiments do not correspond very well to theoretical values, but more important the figures show that there is no correlation between the depletion voltage found after irradiation and the initial depletion voltage. The experiments are therefore in agreement with the theory in that the depletion voltage after irradiation is independent of initial measured values, and that all detectors irradiated to the same fluence have approximately the same depletion voltage. The conclusion is therefore that the pre-irradiation measurements are useless as indicators of the irradiated high restivity detectors depletion voltage.

In figure 5.9 it is possible to compare different set of diodes. Each set consist of three or four diodes of which two was treated with shorter or longer gettering. From figure 5.9 a) and figure 5.9 c) it could be argued that the diodes that received the shortest gettering have the lowest depletion voltage, but when figure 5.9 d) is considered together with the two other plots it is more obvious that this is not correct. The spread in depletion voltage values for identical diodes are of the same order of magnitude as the difference between the non-identical ones. The same spread in values can be seen in table 6.8 for the detectors. When trying to compare diodes with the same gettering, but with different phosphorous implantation the same spread is observed. The conclusion of these depletion voltage measurements

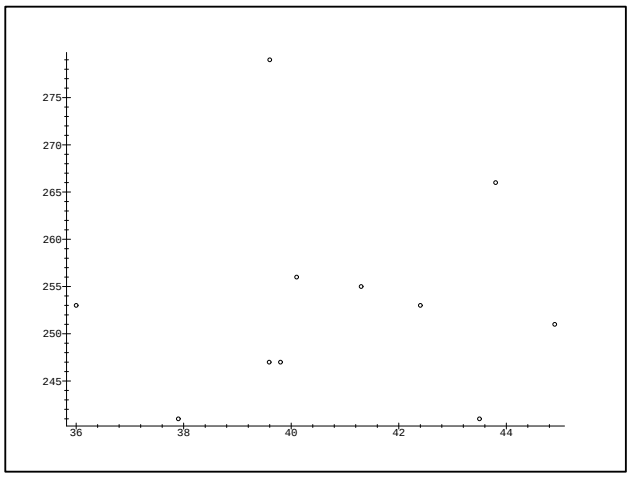

Figure 7.1: V_{dep} for irradiated diodes vs. their full depletion voltage before irradiation

must therefore be that it is not very probable that variations in gettering and concentration of implanted phosphorous can alter the full depletion voltage of a highly irradiated detector.

7.3 Leakage current

The measurements of leakage current gave results that were expected from theory. An increase in J_V immediately after irradiation with a following annealing behaviour was observed. The leakage current was normalized to $20°C$ and calculations of α, the damage constant, were done. From equation 3.24 and a fluence of 3.3×10^{14} protons/cm^2 α was found to be in the range $1.12 - 8.06 \times 10^{-17} Acm^{-1}$. This value is in agreement with earlier published values[15]. It was also tried to calculate α for the detectors, but the correct volume of the detector has to be known. The number of guard rings that are connected depends on the shape of the depletion region, which again depends on the reverse bias. Since the shape of the depletion region of a inverted detector is unknown the area is unknown too, and for this reason α cannot be calculated. In a piece of $300\mu m$ silicon the leakage current will increase with $1 - 7 \times 10^{-4} A/cm^2$, a value several orders of magnitude larger than the initial leakage current. The initial leakage current is negligible com-

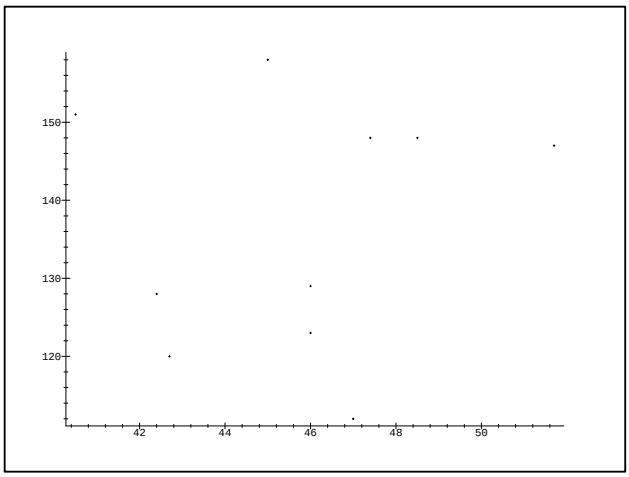

Figure 7.2: V_{dep} for irradiated detectors vs. their full depletion voltage before irradiation

pared to the irradiation induced leakage current, and this is in agreement with chapter 6 where no correlation was found between the irradiated detectors leakage current and the unirradiated detectors leakage current. The conclusion is therefore that the leakage current after irradiation depends on the fluence, and are independent on the the pre-irradiation leakage current.

The same sets of diodes that were analysed in section 7.2 are shown in figure 5.4 and figure 5.5, the sets of the larger diodes in figure 5.6 and figure 5.7. Again there is a large spread in leakage current for diodes that have been treated the same way. Almost all the plots would lead to the conclusion that variations in gettering and phosphorous concentration cannot alter the leakage current of a highly irradiated detector. It is therefore very interesting to look at diodes 9D and 10D in figure 5.4 c) and figure 5.6 c). For this set a significantly lower leakage current was observed for the diodes that received long gettering, 10D, compared to the diodes that received short gettering, 9D. In fact the 10D-diodes have the lowest current of all the small diodes, while the 9D-diodes have the highest. Current of diodes with different phosphorous implantation was also compared, but it was not possible to see any correlation between the current and the phosphorous concentration. The phosphorous concentration can therefore not explain the differences observed between diodes 9D and 10D. Since this effect was not observed for any of the other diodes it is possible that some other property of the material can

be an explanation of why the gettering makes a difference in these samples only. It can therefore be concluded that the length of the gettering might be important for the leakage current if the detector is made of a material with the very specific properties, but gives no effect on other materials.

7.4 Conclusion

A large number of silicon microstrip detectors are to be installed in the ATLAS detector. During the 10 years of operation it will be impossible to replace any of these detectors, and good detectors have therefore to be chosen from the beginning. This can be done in two ways, either the detector is tailor-made to be radiation hard or good detectors are selected from a large number of detectors based on pre-irradiation measurements. These two lines of action have been studied in this thesis, measurements have been done and the data has been discussed qualitatively.

Topic number one was to find out if the processing parameters can alter the electrical properties of a detector after heavy irradiation. For this purpose several diodes and detectors with different processing parameters have been irradiated and tested. The discussions earlier in this chapter have shown that a significant difference in leakage current was seen for only one set of diodes. It was not possible to compare the depletion voltages for this set of diodes, and it was therefore not possible to find out if this effect existed for the depletion voltage too. The difference in leakage current was caused by different gettering length, but was as mentioned not observed for other diodes. It is therefore probable that another property of the detector has to be present to improve the electrical properties. This can be a property of the silicon material or come from the processing. The phosphorous concentration on the backside of the detector is such a property, but was found to have no significant influence on the leakage current or depletion voltage. The conclusion is therefore that it seems possible to influence the electrical performance of a detector after irradiation by choosing the right processing parameters, but that more experiments have to be done to find the necessary initial properties.

Topic number two was to find out if it is possible from the pre-irradiation measurements to foresee the electrical performance after irradiation. The discussions in this chapter have shown that for a typical ATLAS fluence neither the depletion voltage or the leakage current after irradiation can

be predicted from the pre-irradiation measurements, and that they depend mostly on the fluence received.

List of Figures

List of Tables

Bibliography

[1] Atlas calorimeter technical design report, Jan 1997.

[2] Atlas inner detector technical design report, Apr 1997.

[3] Atlas muon spectrometer technical design report, June 1997.

[4] The ROSE Collaboration. Dependece of depletion voltage and capacitance on temperature and frequency in heavily irradiated silicon diodes. *ROSE Technical Note*, 97/4, Mar 1997.

[5] H. Feick et al. Long term damage studies using silicon detectors fabricated from different starting materials and irradiated with neutrons, protons and pions. *Nuclear Instruments and Methods in Physics Research*, A 377:217–223, 1996.

[6] E. Fretwurst et al. Reverse annealing of the effective impurity concentration and long term operational scenario for silicon detectors in future collider experiments. *Nuclear Instruments and Methods in Physics Research*, A 342:119–125, 1994.

[7] Glenn F. Knoll. *Radiation detection and measurement.* John Wiley & Sons, 1989.

[8] W.R. Leo. *Techniques for Nuclear and Particle Physics Experiments.* Springer-Verlag, 1993.

[9] Gunnar Lindstrøm. Private communication, 1998.

[10] D. Morgan, P. Riedler, et al. Analysis of irradiated and annealed atlas prototype silicon detectors. *ATLAS Internal Note*, INDET-NO-209, 1998.

[11] D. Morgan, P. Riedler, et al. Annealing study of irradiated atlas prottype silicon microstrip detectors. *ATLAS Internal Note*, INDET-NO-199, 1998.

[12] Donald A. Neamen. *Semiconductor physics & devices: Basic prinsiples.* IRWIN, 2nd edition, 1997.

[13] Anna Peisert. Silicon microstrip detectors, Jan 1992.

[14] The ROSE Collaboration. *RD48 status report,CERN/LHCC 97-39*, Jun 1997.

[15] The ROSE Collaboration. *2nd RD48 status report,CERN/LHCC 98-39*, Oct 1998.

[16] H. J. Ziock et al. Temperature dependence of the radiation induced change of depletion voltage in silicon pin detectors. *Nuclear Instruments and Methods in Physics Research*, A 342:96–104, 1994.